The Astrophysical Journal Letters, 970:L2 (20pp), 2024 July 20 https://doi.org/10.3847/2041-8213/ad5afa

Transmission Spectroscopy of the Habitable Zone Exoplanet LHS 1140 b with JWST/NIRISS

Charles Cadieux[1], René Doyon[1,2], Ryan J. MacDonald[3,17], Martin Turbet[4,5], Étienne Artigau[1,2], Olivia Lim[1], Michael Radica[1], Thomas J. Fauchez[6,7,8], Salma Salhi[1], Lisa Dang[1], Loïc Albert[1], Louis-Philippe Coulombe[1], Nicolas B. Cowan[9,10], David Lafrenière[1], Alexandrine L'Heureux[1], Caroline Piaulet-Ghorayeb[1], Björn Benneke[1], Ryan Cloutier[11], Benjamin Charnay[12], Neil J. Cook[1], Marylou Fournier-Tondreau[13], Mykhaylo Plotnykov[14], and Diana Valencia[15,16]

[1] Institut Trottier de recherche sur les exoplanètes, Université de Montréal, 1375 Ave Thérèse-Lavoie-Roux, Montréal, QC H2V 0B3, Canada; charles.cadieux.1@umontreal.ca
[2] Observatoire du Mont-Mégantic, Université de Montréal, Montréal, QC H3C 3J7, Canada
[3] Department of Astronomy, University of Michigan, 1085 S. University Ave., Ann Arbor, MI 48109, USA
[4] Laboratoire de Météorologie Dynamique/IPSL, CNRS, Sorbonne Université, Ecole Normale Supérieure, PSL Research University, Ecole Polytechnique, 75005 Paris, France
[5] Laboratoire d'astrophysique de Bordeaux, Univ. Bordeaux, CNRS, B18N, allée Geoffroy Saint-Hilaire, 33615 Pessac, France
[6] NASA Goddard Space Flight Center, 8800 Greenbelt Road, Greenbelt, MD 20771, USA
[7] Integrated Space Science and Technology Institute, Department of Physics, American University, Washington, DC 20016, USA
[8] NASA GSFC Sellers Exoplanet Environments Collaboration, 8800 Greenbelt Road, Greenbelt, MD 20771, USA
[9] Department of Earth & Planetary Sciences, McGill University, 3450 rue University, Montréal, QC H3A 0E8, Canada
[10] Department of Physics and Trottier Space Institute, McGill University, Montréal, QC H3A 2T8, Canada
[11] Department of Physics & Astronomy, McMaster University, 1280 Main St. W, Hamilton, ON L8S 4L8, Canada
[12] LESIA, Observatoire de Paris, Université PSL, CNRS, Sorbonne Université, Université Paris-Cité, 5 place Jules Janssen, 92195 Meudon, France
[13] Atmospheric Oceanic and Planetary Physics, Department of Physics, University of Oxford, OX1 3PU, UK
[14] Department of Physics, University of Toronto, Toronto, ON M5S 3H4, Canada
[15] Department of Physical & Environmental Sciences, University of Toronto at Scarborough, Toronto, ON M1C 1A4, Canada
[16] David A. Dunlap Dept. of Astronomy & Astrophysics, University of Toronto, 50 St. George Street, Toronto, ON M5S 3H4, Canada
Received 2024 May 23; revised 2024 June 19; accepted 2024 June 20; published 2024 July 10

Abstract

LHS 1140 b is the second-closest temperate transiting planet to Earth with an equilibrium temperature low enough to support surface liquid water. At $1.730 \pm 0.025\,R_{\oplus}$, LHS 1140 b falls within the radius valley separating H_2-rich mini-Neptunes from rocky super-Earths. Recent mass and radius revisions indicate a bulk density significantly lower than expected for an Earth-like rocky interior, suggesting that LHS 1140 b could be either a mini-Neptune with a small envelope of hydrogen (∼0.1% by mass) or a water world (9%–19% water by mass). Atmospheric characterization through transmission spectroscopy can readily discern between these two scenarios. Here we present two JWST/NIRISS transit observations of LHS 1140 b, one of which captures a serendipitous transit of LHS 1140 c. The combined transmission spectrum of LHS 1140 b shows a telltale spectral signature of unocculted faculae (5.8σ), covering ∼20% of the visible stellar surface. Besides faculae, our spectral retrieval analysis reveals tentative evidence of residual spectral features, best fit by Rayleigh scattering from a N_2-dominated atmosphere (2.3σ), irrespective of the consideration of atmospheric hazes. We also show through Global Climate Models (GCMs) that H_2-rich atmospheres of various compositions (100×, 300×, 1000× solar metallicity) are ruled out to $>10\sigma$. The GCM calculations predict that water clouds form below the transit photosphere, limiting their impact on transmission data. Our observations suggest that LHS 1140 b is either airless or, more likely, surrounded by an atmosphere with a high mean molecular weight. Our tentative evidence of a N_2-rich atmosphere provides strong motivation for future transmission spectroscopy observations of LHS 1140 b.

Unified Astronomy Thesaurus concepts: Exoplanets (498); Habitable planets (695); Planetary atmospheres (1244); Super Earths (1655); Ocean planets (1151); Mini Neptunes (1063); M dwarf stars (982); Transmission spectroscopy (2133)

Materials only available in the online version of record: machine-readable table

1. Introduction

Whether temperate rocky planets orbiting low-mass stars have an atmosphere is arguably one of the most important scientific questions of the James Webb Space Telescope (JWST) mission (Gardner et al. 2023), one that can only be answered if a significant fraction of its lifetime is dedicated to this endeavor (Cowan et al. 2015; de Wit et al. 2023; Doyon 2024). Answering this question is an essential first step in assessing the habitability of nearby worlds and identifying the best targets for biosignature searches. The first 18 months of JWST observations have highlighted both its power and versatility for studying the atmospheres of small exoplanets. While the first atmospheric reconnaissance of TRAPPIST-1 b (Greene et al. 2023) and TRAPPIST-1 c (Zieba et al. 2023) through eclipse photometry suggests that those two planets may be airless worlds, the

[17] NHFP Sagan Fellow.

presence of atmospheres on these planets has not been definitively ruled out (Ducrot et al. 2023; Ih et al. 2023; Lincowski et al. 2023; Turbet et al. 2023; Zieba et al. 2023). The first JWST transmission spectra of the TRAPPIST-1 planets, in general, show strong signs of stellar activity in the form of continuum variability, unocculted spots/faculae (Lim et al. 2023), and flares (Howard et al. 2023). Unocculted spots/faculae, responsible for the transit light source (TLS) effect (Rackham et al. 2018), pose a significant challenge, as they can mimic genuine atmospheric signals, greatly complicating the interpretation of transmission spectra. The TLS effect is a recurrent theme of numerous Cycle 1 and Cycle 2 transmission spectroscopy programs (e.g., Lim et al. 2023; May et al. 2023; Moran et al. 2023; Fournier-Tondreau et al. 2024), a fundamental problem that has yet to be solved.

LHS 1140 (Dittmann et al. 2017; Ment et al. 2019; Lillo-Box et al. 2020; Cadieux et al. 2024) is a keystone system for habitability studies. This M4.5 dwarf (Dittmann et al. 2017) hosts two small transiting planets: an outer planet LHS 1140 b ($R_p = 1.73\ R_\oplus$), a rare object in the middle of the radius valley (Fulton et al. 2017, 2018; Cloutier & Menou 2020) on a 24.7-day temperate orbit, and an inner planet LHS 1140 c, a warm super-Earth ($R_p = 1.27\ R_\oplus$) orbiting every 3.78 days. The two planets receive 0.43 and 5.3 times the irradiation of Earth, respectively, with LHS 1140 b comfortably situated within the water condensation zone (Turbet et al. 2023). Cadieux et al. (2024) recently presented a joint study of almost all transit and radial velocity observations to date, obtaining a precision of 3% on the masses and 2% on the radii of LHS 1140 b and c. Among the temperate rocky exoplanets, only those in the TRAPPIST-1 system are currently characterized to such precision. Their analysis of the composition of LHS 1140 b shows that the planet could be enveloped in hydrogen (~0.1% H/He by mass), akin to a smaller version of the temperate mini-Neptune K2-18 b, which has a transmission spectrum characterized by prominent CH_4 and CO_2 absorption bands in the near-infrared (Madhusudhan et al. 2023). Alternatively, LHS 1140 b could be a water world with a surface layer of condensed water representing 9%–19% of the total mass. A 3D Global Climate Model (GCM) of the water-world scenario predicts liquid water at the substellar point for a large range of atmospheric compositions (Cadieux et al. 2024). The GCM also predicts a distinctive transmission spectrum featuring relatively small (~15 ppm) CO_2 features at ~2.8 and ~4.3 μm.

Transmission spectroscopy with Hubble Space Telescope (HST)/WFC3 shows a tentative signal of H_2O/CH_4 near 1.4 μm in a low mean molecular weight atmosphere (Edwards et al. 2021; Biagini et al. 2024), but a combination of unocculted spots and faculae offers an alternative explanation —a hypothesis also supported by ground-based measurements (Diamond-Lowe et al. 2020). These observations imply a large fractional coverage (>80%) of stellar active regions, which is somewhat surprising given that LHS 1140 is a relatively old (>5 Gyr; Cadieux et al. 2024), slowly rotating star ($P_{\rm rot} = 131 \pm 5$ days; Dittmann et al. 2017), with low levels of flaring activity (Medina et al. 2022). Recent observations of two transits of LHS 1140 b with JWST/NIRSpec (G235H/G395H, 1.7–5.2 μm) ruled out an H_2-rich atmosphere and favored a high mean molecular weight atmosphere (Damiano et al. 2024). Further TLS characterization with JWST is required, especially in the context of seeking the detection of small atmospheric signals that could be severely affected/biased by stellar activity.

This Letter presents the results of a transmission spectroscopy program with JWST NIRISS/SOSS (0.6–2.8 μm) aimed at both characterizing the stellar activity of LHS 1140 and providing a strong discriminating test of the mini-Neptune/water-world scenarios of Cadieux et al. (2024). We show that the TLS effect is clearly detected in LHS 1140 and that a cloud-free mini-Neptune atmosphere for LHS 1140 b is strongly excluded.

This Letter is structured as follows. The observations and data reduction steps are presented in Section 2, followed by the transit modeling in Section 3 and spectral extraction analysis in Section 4. The retrieved atmospheric properties of LHS 1140 b and TLS constraints are presented and discussed in Section 5, followed by a discussion of proposed follow-up observations in Section 6. We then conclude in Section 7.

2. Observations

Two transits of LHS 1140 b were obtained with JWST using the NIRISS instrument (Doyon et al. 2023) on UT2023-12-01 and UT2023-12-26 as part of program DD6543 (PI: Cadieux & Doyon). The spectroscopic time series were carried out using the SOSS mode (Albert et al. 2023), offering a spectral resolution $R \approx 650$, with the SUBSTRIP256 subarray configuration to access the first two diffraction orders of NIRISS (0.6–2.8 μm). Each visit comprised 949 integrations, covering 2.58 hr before ingress, the 2.15 hr transit, and 1.11 hr after egress. The second visit fully captured a transit of LHS 1140 c lasting 1.13 hr and starting approximately 34 minutes after first contact of LHS 1140 b. Each integration was composed of $n_{\rm group} = 3$, filling approximately 50% of the full well to minimize charge migration and nonlinearity effects (Albert et al. 2023). We made use of two independent data reduction pipelines, namely `SOSSISSE` (Lim et al. 2023) and `supreme-SPOON` (Feinstein et al. 2023; Radica et al. 2023; Benneke et al. 2024; Radica et al. 2024), both yielding consistent transmission spectra with a mean (median) absolute deviation of 0.72σ (0.60σ). More details of both pipelines and their comparison are provided in Appendix A. The `SOSSISSE` data products are hereafter used in the analysis.

During the first visit, the star LHS 1140 was erroneously positioned outside the target acquisition field of view, causing a displacement of the orders on the detector with offsets $\Delta x = -157$ pixels (dispersion) and $\Delta y = -12$ pixels (cross-dispersion) relative to their nominal positions. This offset was calculated by comparing the pixel-to-wavelength calibrations derived from the two visits. A modified wavelength solution for the shifted spectral trace was determined through a cross-correlation between the stellar trace and a PHOENIX stellar atmosphere model (Husser et al. 2013), following the procedure described by Feinstein et al. (2023) and Radica et al. (2023). The target acquisition failure is attributable to an incorrect epoch of proper motion entered during scheduling (LHS 1140 is a high-proper-motion target), which means that this sequence was executed with blind guiding from the observatory. Fortunately, this data set can be fully recovered with a small wavelength shift in order 1—0.70–2.67 μm compared to 0.85–2.83 μm during visit 2—and negligible change in order 2.

The first visit is also affected by a background star[18] that overlaps the spectral trace of LHS 1140 for wavelengths below 0.90 μm in order 1 and between 0.60 and 0.75 μm in order 2,

[18] Gaia DR3 2371032989200665984, $G = 16.667$, $d = 274.08$ pc, (Gaia Collaboration et al. 2023).

contaminating the flux at the 1%–2% level. We estimate a spectral type M2.4 ± 0.4V for the contaminant star using the $G - G_{RP}$ calibration of Kiman et al. (2019). The T_{eff} estimate of 3516 K from Gaia DR3 (Gaia Collaboration et al. 2023) is also consistent with an M2V spectral type (Pecaut & Mamajek 2013). We constructed a model of the trace of the contaminant star from an M0V template (WASP-80; GTO 1201, PI: Lafrenière) observed with NIRISS. This template was aligned by maximizing the correlation coefficient between the derivatives in spatial direction x of the template and observations in regions (pixels) where only the contaminant is seen. Once the optimal shift was determined, we computed the amplitude of the contamination pixel by pixel, and we used the median of these amplitudes to scale the template to match the contaminant trace. We then subtracted this contaminant model from the images, leaving flux residuals of the order of 0.1% on the affected pixels of LHS 1140. Such residuals could decrease (dilute) the transit depth of LHS 1140 b by 10 ppm at most. This possible systematics is further mitigated in the next sections by analyzing both visits together, as visit 2 was not affected by a dispersed contaminant.

3. White Light-curve Analysis

One output of `SOSSISSE` is an amplitude time series $a(t)$ that corresponds to broadband flux measurements (details in Appendix A), hereafter referred to as the "white" light curve (WLC). The WLC is modeled with two components, one for transits and the other for treating systematic signals, both described below. The fit was performed using the `juliet` framework (Espinoza et al. 2019) that generates transit models with `batman` (Kreidberg 2015) and implements Gaussian process (GP) regression with `celerite` (Foreman-Mackey et al. 2017). The posterior distribution is explored with nested sampling and 500 live points using the `dynesty` package (Speagle 2020) available in `juliet`.

The transit component assumes circular orbits for both planets (Gomes & Ferraz-Mello 2020). The orbital parameters of planet k (k: "b", "c") are the period P_k fixed to the value from Cadieux et al. (2024), the time of inferior conjunction $t_{0,k}$, and the scaled semimajor axis $a_k/R_\star$ that we derive using a common stellar density $\rho_\star$. For $\rho_\star$, we use the same Gaussian prior as in Cadieux et al. (2024) constructed from stellar mass and radius estimates. For all other parameters, we adopt wide uniform priors. The transits of LHS 1140 b and c are parameterized with the planet-to-star radius ratio $R_{p,k}/R_\star$ and the impact parameter b_k. We fit for quadratic limb-darkening parameters q_1 and q_2 defined in Kipping (2013), which ensure physical solutions for values between 0 and 1.

For the systematic component, we use GP regression to model two nuisance signals also reported in other NIRISS data sets (e.g., Coulombe et al. 2023; Benneke et al. 2024; Radica et al. 2024): a beat pattern introduced by the observatory thermal control (McElwain et al. 2023), and correlated structures on the timescale of a few minutes suggestive of stellar granulation (e.g., Kallinger et al. 2014; Grunblatt et al. 2017; Pereira et al. 2019). We use a combination of two simple harmonic oscillator (SHO) kernels in `celerite` to jointly model these systematic signals. We fix the period of the first SHO term to 204 s, corresponding to the dominant periodicity in the out-of-transit fluxes based on its power (highest peak) in the generalized Lomb–Scargle periodogram (Zechmeister & Kürster 2009). We fit for an amplitude σ_{beat} and a quality factor Q_{beat} for this oscillation. As in Radica et al. (2024), we use a critically damped SHO term (Q fixed to $\sqrt{0.5}$) for the granulation-like signal and fit for an amplitude σ_{gra} and a timescale τ_{gra} of this stochastic variation. An extra jitter term σ_{jitter} is added in quadrature to the diagonal of the covariance matrix to account for excess noise. We also fit for a baseline flux and a temporal slope for each visit. We measure slopes of −0.26 and −0.36 ppm minute^{-1} during visits 1 and 2, respectively, a flux variation approximately 20–30 times weaker than observed during the transits of TRAPPIST-1 b with NIRISS (Lim et al. 2023). This is consistent with the fact that LHS 1140 is a slow-rotating star with a flux level remarkably stable over a timescale of a few hours, as also confirmed by TESS (Ricker et al. 2015).

Table 1
Transit and Systematic Parameters Inferred from a Joint Fit of the White Light Curve of Visits 1 and 2

Parameter	Prior	Posterior
	Stellar Parameters	
$\rho_\star$ (g · cm^{-3})	$\mathcal{N}(26.0, 2.6^2)$	$26.7^{+0.3}_{-0.6}$
	Orbital Parameters	
P_b (days)	(fixed)[a]	24.73723
P_c (days)	(fixed)[a]	3.777940
$t_{0,b}$ (BJD –2,460,300)	$\mathcal{U}(4.65, 4.75)$	4.69824(3)
$t_{0,c}$ (BJD –2,460,300)	$\mathcal{U}(4.65, 4.75)$	4.70775(4)
$a_b/R_\star$	(derived)[b]	$95.2^{+0.4}_{-0.7}$
$a_c/R_\star$	(derived)[b]	$27.1^{+0.2}_{-0.3}$
	Transit Parameters	
$R_{p,b}/R_\star$ (%)	$\mathcal{U}(0, 50)$	7.439 ± 0.015
$R_{p,c}/R_\star$ (%)	$\mathcal{U}(0, 50)$	5.312 ± 0.028
b_b	$\mathcal{U}(0, 0.9)$	$0.14^{+0.05}_{-0.03}$
b_c	$\mathcal{U}(0, 0.9)$	$0.09^{+0.06}_{-0.06}$
q_1	$\mathcal{U}(0, 1)$	0.16 ± 0.02
q_2	$\mathcal{U}(0, 1)$	0.22 ± 0.05
	GP Parameters	
σ_{beat} (ppm)	$\mathcal{LU}(0.1, 1000)$	69 ± 6
Q_{beat}	$\mathcal{LU}(0.1, 1000)$	$11.3^{+3.4}_{-2.4}$
σ_{gra} (ppm)	$\mathcal{LU}(0.1, 1000)$	53 ± 5
τ_{gra} (min)	$\mathcal{LU}(1, 100)$	5.2 ± 1.0
σ_{jitter} (ppm)	$\mathcal{LU}(0.1, 1000)$	95 ± 3

Notes.
[a] Period from Cadieux et al. (2024).
[b] Scaled semimajor axis ($a/R_\star$) derived from $\rho_\star$ and P.

The WLCs of the two visits were jointly fit with a common $\rho_\star$, q_1, and q_2 to allow more precise constraints. The adopted priors and resulting posteriors (16th, 50th, and 84th percentiles) of this fit are presented in Table 1. The best-fit transit and systematic components of the WLC are shown in the top panels of Figure 1. Fitting visit 1 and visit 2 independently yielded consistent parameters within the 1σ uncertainty, but we note a systematic increase of ∼40 ppm in the transit depth of LHS 1140 b during visit 2 due to the double transit. The joint fit alleviates the covariance between $R_{p,b}$, $R_{p,c}$, and b_c in visit 2 by using the information of a single transit of planet b from visit 1. This same argument is later used to extract combined transmission spectra of LHS 1140 b and c by jointly fitting the two visits in each spectral channel.

4. Spectrophotometric Analysis

We binned the extracted spectroscopic time series from `SOSSISSE` to $R \approx 100$ in both order 1 and order 2. We

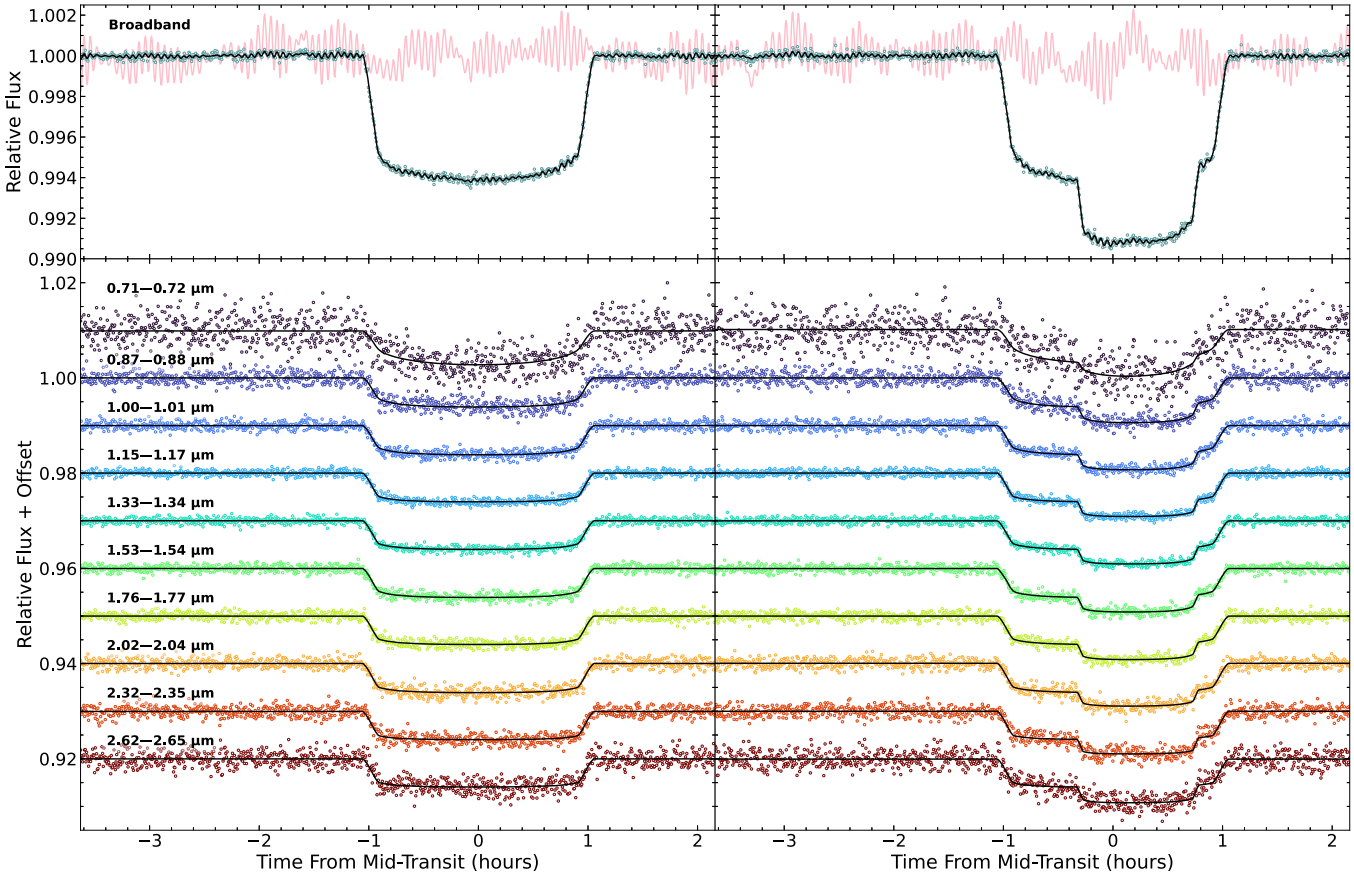

Figure 1. Spectrophotometric transit fits of LHS 1140 b for visit 1 (UT2023-12-01; left) and visit 2 (UT2023-12-26; right) and LHS 1140 c for visit 2 only. The broadband ("white") light curves are shown in the top panels, with the best-fit full model (transit + systematics) shown in black and systematics component only in pink (scaled 10× for clarity). For both visits, examples of 10 systematics-corrected spectroscopic bins are depicted with colored points in the bottom panels.

excluded wavelengths below (above) 0.86 μm in spectral order 1 (2), as these wavelengths are already covered by the other order at a higher throughput. Because of the wavelength coverage differing between the two data sets (see Section 2), this results in 145 spectrophotometric light curves for the first visit and 149 for the second visit. We also constructed a common wavelength grid at the native resolution corresponding to the average of the nearest pixels (in wavelength) between the two visits. This average grid deviates at most by 0.23 nm from the wavelength calibrations from individual visits. We combined the spectral time series of visit 1 and visit 2 using the common wavelength grid and then binned to an $R \approx 100$ to end up with 142 joint spectrophotometric light curves. We then removed the systematic component determined from the WLC from all spectral light curves. At $R \approx 100$, the median photometric precision of the light curves is approximately 800 ppm, which prevents us from characterizing the beat pattern and granulation signals, both with amplitudes below 100 ppm (Table 1).

To derive the transmission spectra of LHS 1140 b and c, we fitted a transit model to each spectrophotometric light curve. Again, the fits were carried out with `juliet` using nested sampling and 500 live points for each spectral bin. We fixed P_k, $t_{0,k}$, $a_k/R_\star$, and b_k to the best-fit values from the WLC analysis (Table 1) and fit for $R_{p,k}/R_\star$. The limb-darkening coefficients were calculated for all spectral channels with `ExoTic-LD` (Grant & Wakeford 2022) using a custom PHOENIX model input ($T_{\rm eff} = 3100$ K, $\log g = 5$, [Fe/H] = 0.0) for LHS 1140. For the spectral fits, the corresponding q_1 and q_2 limb-darkening parameters are kept fixed. We allow for a baseline flux parameter and a $\sigma_{\rm jitter}$ for each visit and all spectroscopic bins. Examples of 10 spectroscopic channels jointly fitting the transits of LHS 1140 b and c are shown in Figure 1.

The final combined transit spectrum of LHS 1140 b is presented in Figure 2, along with a binned version at $R \sim 20$ to ease comparison with HST/WCF3 data. The spectrum is relatively flat above 1 μm but features a clear 200 ppm decrease toward shorter wavelengths. We show in the next section that this is a signature of the TLS effect from unocculted faculae. The HST/WFC3 data are fairly consistent with NIRISS, albeit for one or two data points with larger transit depth blueward of 1.4 μm that may have largely contributed to the tentative water/methane detection mentioned by Edwards et al. (2021) and Biagini et al. (2024). The transmission spectra of LHS 1140 b and c are available in Appendix B.

5. The Atmosphere of LHS 1140 b

We now use the combined transmission spectrum of LHS 1140 b to jointly infer properties of the planetary atmosphere and stellar contamination from unocculted active regions resulting in stellar contamination (the TLS effect). Our analysis considers the evidence for stellar contamination (Section 5.1), evidence for a planetary atmosphere through retrievals (Section 5.2), and finally a comparison with GCM predictions of mini-Neptunes (Section 5.3). We also provide a preliminary analysis of the transmission spectrum of LHS 1140 c in

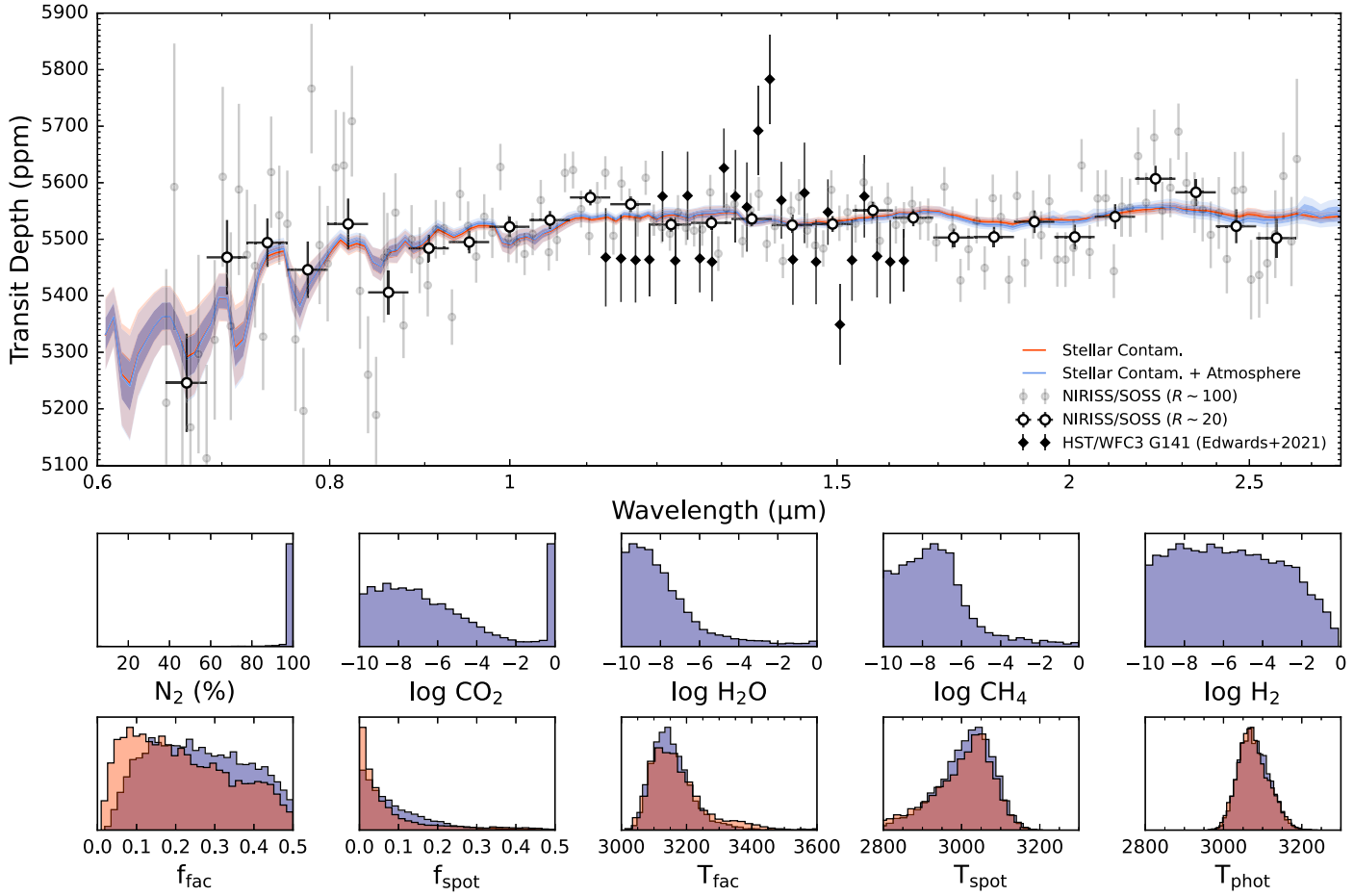

Figure 2. Combined transmission spectrum of LHS 1140 b with NIRISS/SOSS from two transits and POSEIDON retrieval analysis results. The binned spectra at $R \sim 20$ (white points) and at a higher $R \sim 100$ (gray points) significantly improve on the HST/WFC3 data from Edwards et al. (2021; black diamonds). The median models with 1σ–2σ confidence envelopes are shown for a stellar contamination model (orange) and a joint stellar contamination and planetary atmosphere model (blue), with their respective posterior distributions shown in the bottom panels (same colors). Confidence intervals for each parameter are given in Table D1. The transmission spectrum of LHS 1140 b is mainly shaped by stellar contamination from unocculted faculae. A planetary atmosphere dominated by N_2 or CO_2 is compatible with the data, with the former pure composition being the maximum a posteriori model. A clear N_2-rich atmosphere combined with unocculted faculae is preferred at 2.3σ over faculae alone (see Section 5.2 and Figure D1).

Appendix C, showing that its spectrum is featureless and inconsistent with a cloud-free H_2-rich atmosphere.

5.1. Transit Light Source Effect from LHS 1140

We first consider whether LHS 1140 b's transmission spectrum can be explained only by unocculted stellar active regions. We modeled the TLS effect using the transmission spectra stellar contamination module of the `POSEIDON` retrieval package (MacDonald & Madhusudhan 2017; MacDonald 2023). We generate model spectra by multiplying a bare-rock transmission term, $(R_p/R_\star)^2$, by the wavelength-dependent stellar contamination factor from two distinct stellar heterogeneities (Equation (3) in Fournier-Tondreau et al. 2024). The active region spectra are calculated by interpolating PHOENIX stellar models using the `PyMSG` package (Townsend & Lopez 2023). Our TLS model fits for the covering fractions and temperatures of the facula, spot, and quiet photosphere, yielding six free parameters: R_p, $f_{\rm fac}$, $f_{\rm spot}$, $T_{\rm fac}$, $T_{\rm spot}$, and $T_{\rm phot}$. We fix the surface gravity of all active regions to $\log g = 5.04$ (Cadieux et al. 2024). The priors are listed in Table D1 and mainly follow those in Fournier-Tondreau et al. (2024) for their two-heterogeneity model. Our `POSEIDON` model spectra are generated at $R = 20{,}000$ from 0.60 to 2.9 μm, convolved with a Gaussian kernel to the native resolution of NIRISS/SOSS ($R \approx 650$), and then multiplied by the instrument sensitivity function and binned down to the wavelength spacing of the data ($R \approx 100$). The parameter space is explored via the nested sampling package `PyMultiNest` (Feroz & Hobson 2008; Buchner et al. 2014) with 2000 live points. The posterior distributions for this TLS-only model are shown in orange in the bottom row of Figure 2 (also in Appendix D), with the median and 1σ confidence intervals listed in Table D1.

LHS 1140 b's transmission spectrum shows definitive evidence of unocculted stellar faculae. We detect faculae at 5.8σ confidence ($\Delta \ln \mathcal{Z} = 14.91$, where $\Delta \ln \mathcal{Z}$ is the increase in log Bayesian evidence for stellar contamination over a flat line). Our six-parameter TLS model ($\chi^2_\nu = 1.73$, with 136 degrees of freedom), shown in Figure 2, provides a significantly better fit compared to a flat line ($\chi^2_\nu = 1.96$, with 141 degrees of freedom). The reduced χ^2 of 1.73 may be indicative of underestimated error bars, or perhaps imperfect TLS modeling due to inherent uncertainties in stellar atmosphere models (Lim et al. 2023; Jahandar et al. 2024). We find unocculted faculae 72^{+84}_{-32} K hotter than the photosphere covering $20\%^{+17\%}_{-12\%}$ of the visible stellar disk. There is no evidence for spots. A wide range of covering fractions are consistent with

the data, due to the degeneracy between $f_{\rm fac}$ and $\Delta T = T_{\rm fac} - T_{\rm phot}$ (i.e., smaller/larger faculae need to be hotter/cooler to produce a similar spectral contamination). This level of stellar activity is consistent, within a factor of order unity, with the observed photometric peak-to-peak variability of ∼1% of LHS 1140 (Dittmann et al. 2017) inferred from a 2 yr monitoring campaign with MEarth (Irwin et al. 2009).

We note that fitting a single stellar contamination model to LHS 1140 b's combined spectrum amounts to assuming a similar surface distribution of unocculted heterogeneities during the times of the two visits separated by one orbital period of 24.7 days, equivalent to ∼20% of one stellar rotation. To validate this assumption, we also fit the same TLS-only model to the transmission spectrum of each individual visit, obtaining $f_{\rm fac} = 0.18^{+0.16}_{-0.11}$ and $T_{\rm fac} = 3151^{+77}_{-54}$ K for visit 1 and $f_{\rm fac} = 0.06^{+0.16}_{-0.03}$ and $T_{\rm fac} = 3420^{+237}_{-227}$ K for visit 2. We also observe consistent unocculted faculae properties from LHS 1140 c's transmission spectrum with $f_{\rm fac} = 0.12^{+0.18}_{-0.07}$ and $T_{\rm fac} = 3293^{+205}_{-111}$ K during visit 2 (Appendix C). This confirms that our two visits have consistent faculae properties, and hence it is valid to analyze the combined spectrum with a single TLS model. The consistent facula parameters from our LHS 1140 b and LHS 1140 c analyses confirm that these unocculted faculae lie outside the stellar surface sampled by the two planetary transit chords. We additionally note that Damiano et al. (2024) reported a spot-crossing event during a different set of two transits of LHS 1140 b observed with NIRSpec in 2023 July. Their observations, conducted 124 days prior to our NIRISS data set (about one full rotation of LHS 1140), disfavor unocculted heterogeneities (their Table 4). However, the longer wavelengths covered by NIRSpec G235H and G395H are less sensitive to the TLS effect. Our analysis therefore critically underscores the need for NIRISS observations to characterize the nature and spectral impact of unocculted stellar active regions on transmission spectra.

5.2. Atmospheric Retrieval

We next establish whether there is any evidence of an atmosphere on LHS 1140 b. Given the presence of unocculted faculae established above, we performed a joint stellar contamination and planetary atmosphere retrieval analysis using `POSEIDON`. We consider a range of atmospheric retrieval models, including single-gas pure atmospheres, multiple gases, and atmospheres with or without aerosols. Our models consider the following gases (opacity sources in parentheses): CO_2 (Tashkun & Perevalov 2011), H_2O (Polyansky et al. 2018), CH_4 (Yurchenko et al. 2017), H_2 (Hohm 1994 for Rayleigh scattering; Karman et al. 2019 for collision-induced absorption (CIA)), and N_2 (Sneep & Ubachs 2005 for Rayleigh scattering; Karman et al. 2019 for CIA). For multigas models, the volume mixing ratios follow a permutation-invariant centered-log-ratio (CLR) prior (Benneke & Seager 2012), which allows for any molecule to be equally likely a priori to be the dominant gas. We assume isothermal atmospheres and fit for a reference radius, $R_{p,\rm ref}$, at a reference pressure of 1 bar. We include a two-parameter power-law prescription for hazes (MacDonald & Madhusudhan 2017) in all multigas atmospheric models. For the cloudy model, we assume an optically thick gray opacity/surface with all layers deeper than $P_{\rm surf}$ set to infinite opacity. We allow M_p to vary as a free parameter following a Gaussian prior ($5.60 \pm 0.19\ M_\oplus$; Cadieux et al. 2024). For the stellar contamination, we use the same TLS parameterization as outlined above (i.e., five parameters to fit for both faculae and spots). We used 2000 `PyMultiNest` live points for all retrievals. A summary of the free parameters and their priors is provided in Table D1.

Our retrieval analysis identifies tentative evidence for a cloud-free N_2-dominated atmosphere on LHS 1140 b (2.3σ). We first considered models with a single-gas atmosphere with negligible cloud opacity in the upper atmosphere (all including stellar contamination), finding that the fit did not improve for CO_2, H_2O, CH_4, or H_2 pure atmospheres. For example, our 100% CO_2 model has a lower Bayesian evidence compared to stellar contamination only ($\ln \mathcal{Z} = 1141.02$ vs. 1142.15)—reflecting the "Occam penalty" from adding one or more parameters that do not improve the fit (see, e.g., Trotta 2008)—since there are no apparent CO_2 features in our NIRISS spectrum. Pure CO_2 atmospheres must have $T < 233$ K (2σ upper limit) to be compatible with our nondetection of CO_2 absorption (i.e., high-temperature pure CO_2 atmospheres are ruled out). However, our 100% N_2 model has the highest Bayesian evidence of all our models ($\ln \mathcal{Z} = 1144.65$), with a $\Delta \ln \mathcal{Z} = 2.50$ (2.8σ) for N_2 + stellar contamination over stellar contamination alone. The evidence for N_2 arises from a combination of a residual short-wavelength slope compatible with N_2 Rayleigh scattering and a weak feature near 2.2 μm attributable to N_2–N_2 CIA—see Appendix D and Figure D1. Our multiple gas retrieval reaffirms that N_2 is the favored background gas, even when hazes are included in the model, with a retrieved abundance of $100\%^{+0\%}_{-2\%}$ (see Figure 2, blue posteriors), indicating that our data rule out the tail to lower N_2 abundances present in the CLR prior. We rule out cloud-free H_2O-rich, CH_4-rich, and H_2-rich atmospheres, with 2σ upper limits of $\log H_2O < -2.94$, $\log CH_4 < -2.78$, and $\log H_2 < -0.95$ (<11%), respectively. While our multiple gas retrieval does allow for cold ($T \approx 100$ K) CO_2-rich atmospheres (corresponding to a relatively featureless atmospheric contribution to the spectrum), this solution is not statistically favored, as discussed above. To provide a more conservative estimate for the N_2 detection significance, we calculated the Bayesian evidence for a multiple gas model including all the other gases and hazes but without N_2 (ensuring that the possibility of both CO_2-dominated atmospheres and hazes is propagated into the Bayesian evidence), finding a conservative $\Delta \ln \mathcal{Z} = 1.50$ (2.3σ) in favor of a N_2-dominated atmosphere. Our tantalizing evidence for a N_2-dominated atmosphere on a habitable-zone super-Earth raises a resounding call for additional observations of LHS 1140 b to confirm this result.

We additionally considered the potential for aerosols in LHS 1140 b's atmosphere. First, we reiterate that our multigas retrieval discussed above included a parametric prescription for atmospheric hazes (MacDonald & Madhusudhan 2017). The haze parameters are unconstrained in all our retrievals (see posteriors in Appendix D). The reason for this is that hazes still exist within an atmosphere, providing an additional opacity enhancing the dominant Rayleigh slope, but the retrieval must first "select" a background gas before the impact of a haze can be established. If N_2 is the background gas, N_2 Rayleigh scattering alone provides a good fit, and additional haze opacity is not needed (hazes are redundant parameters). If CO_2 is the dominant gas, then hazes have no spectral effect, due to the high molecular weight and low temperature shrinking the scale height and hence flattening the spectrum. Therefore, allowing for hazes does not affect the inference of a clear N_2-dominated atmosphere as the favored model. When we include a cloud/

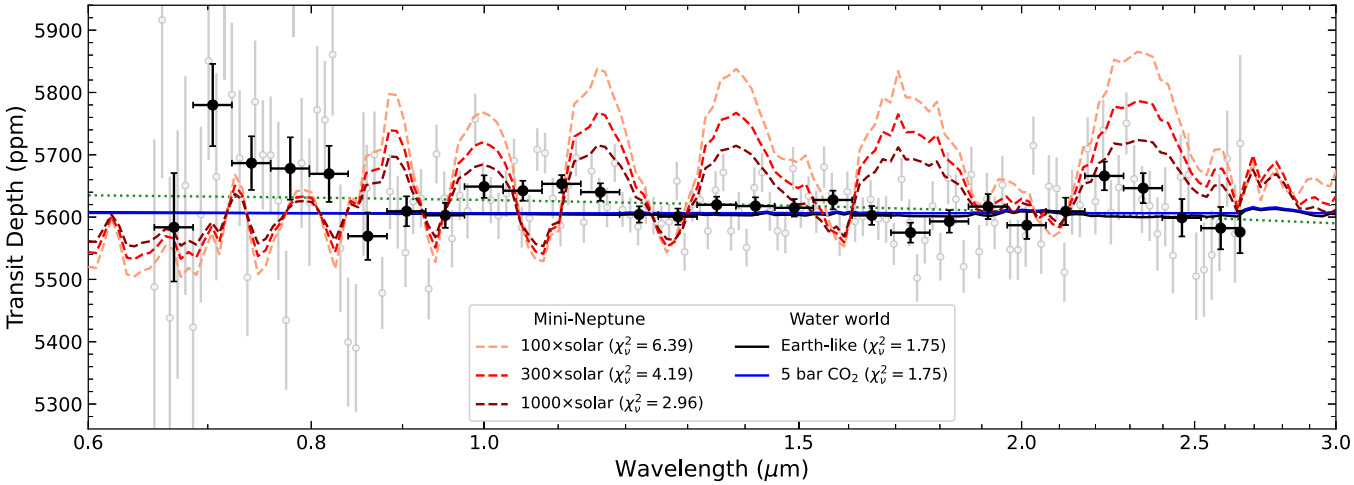

Figure 3. Stellar-contamination-corrected combined spectrum of LHS 1140 b using the best-fit solution of Figure 2. The black points are binned to $R \sim 20$, while the gray points are at a higher $R \sim 100$. Dashed lines depict GCM-based forward models produced with PSG for a mini-Neptune atmosphere (100×, 300×, 1000× solar metallicity), and solid lines depict the water-world GCMs of Cadieux et al. (2024) for an Earth-like atmosphere (1 bar N_2, 400 ppm CO_2) and a pure CO_2 atmosphere at 5 bars. An H_2-rich atmosphere for LHS 1140 b is formally rejected ($>10\sigma$) by the NIRISS/SOSS data. A flat solution (e.g., water world or airless planet) provides a significantly better fit, but the reduced χ^2 of 1.75 may indicate an underestimation of error bars, an imperfect TLS correction, or the presence of residual spectral features (e.g., slope). An apparent linear trend with a slope of approximately 40 ppm across the NIRISS domain (dotted green line) improves the fit ($\chi^2_\nu = 1.72$) but is not predicted by our GCMs.

surface in our multigas retrieval, we obtain a bimodal solution: (i) a clear ∼100% N_2 atmosphere, as above, or (ii) an optically thick cloud deck at low $P_{\rm surf} \sim 10^{-5}$ bar with no constraints on the atmospheric composition (i.e., such high-altitude clouds would render any transmission spectrum featureless, regardless of the atmospheric composition). The Bayesian evidence decreases when adding a cloud deck (see Table D1), indicating that this is a redundant parameter not required to explain LHS 1140 b's transmission spectrum. We also stress that such exceedingly high altitude clouds are probably unrealistic. According to 3D GCMs of LHS 1140 b for both the water-world (Cadieux et al. 2024) and hydrogen-rich scenarios (see below), a cloud deck (e.g., H_2O, CO_2 clouds) should form much deeper in the atmosphere ($P \approx 1$ bar). Therefore, while our present observations do not strongly favor a clear N_2-dominated atmosphere over a high-altitude cloud deck, the latter scenario is less plausible from a GCM standpoint.

We examine the evidence for N_2 in the atmosphere of LHS 1140 b and present our full atmospheric retrieval results and posterior distributions in Appendix D.

5.3. 3D GCM Forward Modeling

Here we compare the observed spectrum with realistic predictions from 3D GCMs of a mini-Neptune with an 80-bar H_2-rich atmosphere of various compositions: 100×, 300×, and 1000× solar metallicity. For this, we used the Generic Planetary Climate Model (PCM), historically known as the Generic LMD GCM, as in Cadieux et al. (2024). The model is capable of simulating various types of exoplanets, including terrestrial planets in the TRAPPIST-1 system (Turbet et al. 2018; Fauchez et al. 2019) and sub-Neptunes such as GJ 1214b (Charnay et al. 2015) and K2-18 b (Charnay et al. 2021). The GCM simulations performed here closely follow the methodology described in Charnay et al. (2021), except that star and planet properties have been adapted to LHS 1140 b. The GCM experiments are described in more detail in Appendix E.

Following the methodology of Fauchez et al. (2019), the outputs of the GCMs are used as inputs to the Planetary Spectrum Generator (PSG; Villanueva et al. 2018) to generate synthetic transmission spectra using the GlobES module (Villanueva et al. 2022) that consider the 3D nature of the atmosphere and cloud in a self-consistent manner. The simulations include atmospheric refraction, CIA, and multiple scattering. Irrespective of atmospheric composition, all GCMs predict a cold trap between ∼0.1 and 1 bar (see Figure E1), favoring condensation of H_2O into clouds. As seen in Figure 3, the mini-Neptune PSG spectra show strong transmission features of CH_4 and CO_2 (to a lesser extent). Figure 3 compares the TLS-corrected transmission spectrum of LHS 1140 b with these realistic cloudy mini-Neptune models, along with water-world GCMs taken from Cadieux et al. (2024) for an Earth-like atmosphere (1 bar N_2, 400 ppm CO_2) and a pure CO_2 atmosphere at 5 bars. All hydrogen-rich GCMs are formally rejected by the data (fitting for an offset) with a confidence level exceeding 10σ, with a $\Delta \ln \mathcal{Z} = -326.90$, -172.22, and -84.98 for the 100×, 300×, and 1000× solar metallicity models, respectively, compared to a flat spectrum. The water-world GCMs or a flat line (airless planet) provide a much better fit to the data. However, we note an apparent slope of ∼40 ppm in the spectrum that is not predicted by the GCMs explored in this study. The possible origin of this residual slope is discussed in Appendix D.

6. Discussion

6.1. A Secondary Atmosphere on LHS 1140 b?

While an exceptionally cloudy mini-Neptune is compatible with our NIRISS spectrum, such a scenario would be in stark contrast with the relatively clear atmospheres predicted by self-consistent GCMs of LHS 1140 b. Recent observations of the temperate mini-Neptunes K2-18 b (Madhusudhan et al. 2023) and TOI-270 d (Benneke et al. 2024) have detected strong spectral features associated with H_2-rich atmospheres, with relatively little cloud opacity. Instead, our tentative inference of a N_2-dominated atmosphere suggests that LHS 1140 b is a water world with a secondary atmosphere (Forget &

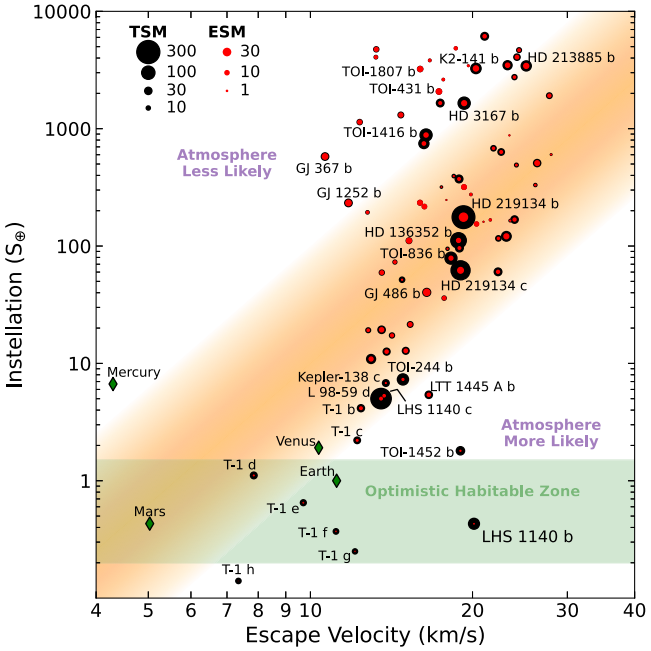

Figure 4. Escape velocity–instellation diagram of small exoplanets ($R_p < 1.8\ R_\oplus$). The empirical "cosmic shoreline" ($S \propto v_{esc}^4$) of Zahnle & Catling (2017) based on solar system bodies is depicted in orange with an arbitrary envelope to underscore uncertainty with spectral types. The size of data points scales with their Transmission and Emission Spectroscopy Metrics (TSM and ESM; Kempton et al. 2018) to highlight favorable targets for JWST atmospheric characterization. Targets with $S < 10\ S_\oplus$ or with TSM/ESM above 90th percentile are annotated. The TRAPPIST-1 system is abbreviated as "T-1." The optimistic habitable zone (early Mars/recent Venus) defined by Kopparapu et al. (2013) is shown in green (approximated for a range of spectral types). With a relatively high escape velocity and low instellation, LHS 1140 b likely retained an atmosphere.

Leconte 2014; Kite & Ford 2018; Kite & Barnett 2020; Marounina & Rogers 2020).

One line of evidence supporting atmospheric retention on LHS 1140 b is that the planet is likely resilient to atmospheric mass loss of light elements (H_2, He) from processes such as extreme UV-driven photoevaporation (Owen & Wu 2017) and core-powered mass loss (Ginzburg et al. 2018). According to Cadieux et al. (2024, their Figure 4), an initial envelope mass fraction as low as ∼0.1% H/He could mostly persist after 10 Gyr thanks to the relatively low instellation of LHS 1140 b combined with its relatively high surface gravity. Based on these results, it is probable that an atmosphere composed of any elements heavier than hydrogen or helium would also be retained by the planet over similar timescales.

Another way to present this argument is illustrated in Figure 4, showing the instellation versus the escape velocity of LHS 1140 b ($S = 0.43 \pm 0.03\ S_\oplus$, $v_{esc} = 20.13 \pm 0.37$ km s^{-1}; Cadieux et al. 2024), along with other exoplanets smaller than $1.8\ R_\oplus$ using the NASA Exoplanet Archive (Akeson et al. 2013). This radius cut is chosen to focus on terrestrials, super-Earths, and potentially water worlds, excluding exoplanets predominantly composed of gas. The empirical "cosmic shoreline" ($S \propto v_{esc}^4$) of Zahnle & Catling (2017) based on solar system objects appears as an orange band in the figure, a region that separates planets with an atmosphere from those without. Reconnaissance atmospheric characterization in transmission and/or in emission with JWST of a few key targets will be required to establish this shoreline across spectral types.

As shown in this diagram, LHS 1140 b, TOI-1452b (Cadieux et al. 2022), TRAPPIST-1 f, and TRAPPIST-1 g (Agol et al. 2021) appear as the most favorable small exoplanets to host a (secondary) atmosphere.

6.2. Future Observations

Considering the significant implications associated with the potential detection of a secondary atmosphere on LHS 1140 b, seeking unambiguous evidence warrants a combined approach of eclipse and transmission spectroscopy. Here we discuss the required observations to ascertain with high certainty the presence of a secondary atmosphere on LHS 1140 b (or lack thereof). It should be noted that, due to the system's limited visibility with JWST, only four or five transits/eclipses of LHS 1140 b are observable in a given year.

6.2.1. Eclipse Photometry

Eclipse photometry centered on the 15 μm CO_2 absorption feature is a powerful tool for constraining the presence of an atmosphere on small rocky planets, e.g., TRAPPIST-1 b (Greene et al. 2023) and TRAPPIST-1 c (Zieba et al. 2023). The eclipse depth is given by $F_p/F_\star$, where F_p and $F_\star$ are, respectively, the flux from the dayside of the planet and the star during the eclipse. Assuming a BT-COND stellar atmosphere model (Allard et al. 2012) with an effective temperature of 3100 K anchored to the Two Micron All Sky Survey J magnitude of LHS 1140, we find $F_\star = 10.1$ mJy for the F1500W MIRI filter. The observations of TRAPPIST-1 b at 15 μm suggest that the stellar model prediction for $F_\star$ should be accurate to ∼10% (Greene et al. 2023). A blackbody is assumed for F_p with the equilibrium temperature $T_{eq} = T_{eff}\ \sqrt{R_\star/a}\ [f(1 - A_B)]^{1/4}$, where T_{eff} is the effective temperature of the host star, $R_\star$ its radius, a the planet semimajor axis, A_B the planet Bond albedo, and f the reradiation factor that can take two extreme values: $f = 1/4$, corresponding to a homogeneous distribution of the energy across the planet, and $f = 2/3$, corresponding to no heat redistribution to the nightside (Esteves et al. 2013).

Figure 5 shows the predicted emission spectrum of LHS 1140 b for two airless models with different albedos and the two water-world GCM cases of Cadieux et al. (2024). We used PSG in the eclipse viewing geometry mode to generate synthetic emission spectra from GCM outputs. Three visits with MIRI would be sufficient to detect/exclude at the 3σ level the most optimistic scenario ($A_B = 0, f = 2/3$) corresponding to a dark, airless planet that is the coreless case inferred from the internal structure model of Cadieux et al. (2024). An airless Europa-like surface ($A_B = 0.6$; Buratti & Veverka 1983) would require ∼19 visits to detect the secondary eclipse, i.e., observing every eclipse for nearly 5 yr. Detecting and discriminating the water-world cases (an Earth-like or CO_2-rich atmosphere) is out of reach through eclipse photometry at 15 μm only and would probably require the combination of many filters (e.g., 15 + 21 μm) over many eclipses.

6.2.2. Transmission Spectroscopy

Cadieux et al. (2024) estimated that 12 transits (six times each of NIRSpec G235 and G395) would be required to detect the CO_2 features longward of 2.8 μm, an exposure time in line with the nine additional G395 visits proposed by Damiano et al. (2024) to detect the CO_2 feature at 4.3 μm. While G395

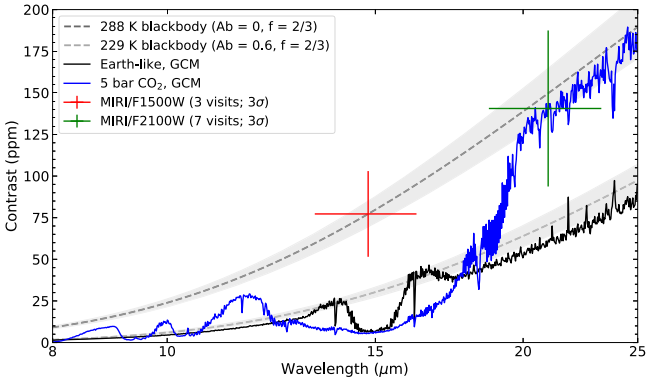

Figure 5. Predicted emission spectrum of LHS 1140 b for various scenarios, including the Earth-like (1 bar N_2, 400 ppm CO_2) and pure CO_2 (5 bars) atmosphere cases from the GCMs of Cadieux et al. (2024). Extreme Bond albedo cases (0 or Europa-like) with no atmospheric heat redistribution ($f = 2/3$) are shown with dashed lines. The gray envelope represents the 10% uncertainty of LHS 1140's stellar flux inferred from a BT-COND model. The red plus sign, centered on the deepest airless case ($A_B = 0, f = 2/3$), gives the predicted uncertainty at 15 μm for three visits needed to reach a 3σ detection assuming photon-limited performance. Similarly, the green plus sign gives the number of visits needed (7) for detecting the deepest eclipse at 21 μm. Each visit is assumed to last ~7.5 hr (1 hr + 3 times the transit duration), a similar experimental design to that adopted by Greene et al. (2023) and Zieba et al. (2023) for the MIRI observations of TRAPPIST-1 b and c, respectively.

may be the most attractive mode for maximizing the signal-to-noise ratio (S/N) of the 4.3 μm feature, it comes with the significant scientific compromise that the atmospheric water abundance in the presence of TLS, as observed in LHS 1140 b, is likely to be poorly constrained. The same ambiguity issue between TLS and water detection associated with the G395 mode alone has been noted by other NIRSpec programs on warm super-Earths (e.g., Moran et al. 2023; May et al. 2023). Moreover, the G395 mode is insensitive to short-wavelength spectral slopes associated with hazes and Rayleigh scattering. Our observations provide tantalizing evidence (2.3σ) for a Rayleigh scattering slope and a CIA feature around 2.2 μm that could be explained by a N_2-rich atmosphere. Such a signal could be confirmed with approximately four additional visits that should also include NIRSpec observations since the N_2–N_2 CIA shows stronger opacity at 4.3 μm, which is very close to the CO_2 feature. Clearly, the optimal experimental design for exploring the full diversity of secondary atmospheres (N_2- or CO_2-rich) along with proper TLS characterization calls for the widest possible wavelength coverage as offered by the combination of NIRISS/SOSS and NIRSpec/G395. Observing within the same season (July or December) through two consecutive visits between NIRISS and NIRSpec minimizes the change in stellar rotation phase, which is only ~20% given the relative orbital period of LHS 1140 b (24.7 days) and the stellar rotation period of ~131 days. The two consecutive transits of LHS 11140 b observed with NIRISS that we presented in this Letter are the proof of concept of this experimental design, showing that the TLS can vary weakly within one observing season, implying that the G395 and NIRISS data acquired within one season could be analyzed jointly under the reasonable assumption that both visits share a similar stellar heterogeneity configuration.

7. Summary and Conclusion

We have presented the 0.65–2.7 μm transmission spectrum of the temperate planet LHS 1140 b obtained from two visits with JWST/NIRISS, the second of which coincidentally involved a transit of LHS 1140 c. All spectra exhibit a low level of stellar contamination caused by unocculted faculae with covering fractions at the level of ~20%. GCMs of mini-Neptunes with various atmospheric compositions (100×, 300×, 1000× solar metallicity) are all excluded with a significance greater than 10σ. A spectral retrieval analysis also excludes a clear H_2-rich atmosphere, with the most likely atmospheric scenario being that of a N_2- or CO_2-dominated envelope. The former N_2-rich atmospheric composition is favored by the data at 2.3σ from a tentative detection of N_2 Rayleigh scattering combined with weak N_2–N_2 CIA absorption near 2.2 μm. While an H_2-rich atmosphere with a relatively high cloud deck is consistent with the NIRISS observations, such a muted spectrum is in contradiction with cloud formation simulated in GCMs and the relatively clear atmospheres detected on the temperate mini-Neptunes K2-18 b (Madhusudhan et al. 2023) and TOI-270 d (Benneke et al. 2024).

The NIRISS observations are more likely consistent with the water-world scenarios presented by Cadieux et al. (2024), with or without a secondary atmosphere, a conclusion also supported by recent transmission spectroscopy data obtained with JWST/NIRSpec (Damiano et al. 2024). Of all nearby small, temperate planets, LHS 1140 b is the most likely to have retained a secondary atmosphere based on its low instellation and high surface gravity. The next obvious step to better constrain LHS 1140 b's atmospheric composition is to perform a joint analysis of both NIRISS and NIRSpec data sets, ideally with a common data reduction methodology.

Only three visits of 15 μm eclipse photometry with MIRI are required to yield a 3σ detection of the secondary eclipse associated with a dark, airless planet, but nearly 5 yr (four to five eclipses per year) are required if its albedo is closer to an icy surface ($A_B \sim 0.5$) as suggested by the relatively high water mass fraction (~15%) of LHS 1140 b. Transmission spectroscopy is the most efficient method to detect the potential secondary atmosphere of LHS 1140 b through consecutive observations between NIRISS/SOSS and NIRSpec/G395 during the same season to allow for a proper characterization of stellar contamination at all epochs and explore N_2- and CO_2-dominated atmospheres. Given the limited visibility of LHS 1140 b, several years worth of observations may be required to detect its potential secondary atmosphere, a program that should be initiated as soon as possible given the limited lifetime of JWST. LHS 1140 b is arguably the best temperate transiting planet for which liquid surface water may be indirectly inferred through the detection of a sufficient level of atmospheric CO_2.

Acknowledgments

We thank the anonymous referee for a very thoughtful report, whose constructive comments and suggestions improved the clarity and quality of the Letter. This work is based on observations made with the NASA/ESA/CSA JWST. The data were obtained from the Mikulski Archive for Space Telescopes at the Space Telescope Science Institute, which is operated by the Association of Universities for Research in Astronomy, Inc., under NASA contract NAS 5-03127 for JWST. These observations are associated with program No. 6543 (doi:10.17909/yf93-zf91). This work is partly supported by the Natural Science and Engineering Research Council of Canada, the Canadian Space Agency, and the Trottier Institute for Research on Exoplanets

(iREx) through the Trottier Family Foundation. This work benefited from support of the Fonds de recherche du Québec—Nature et technologies (FRQNT), through the Center for Research in Astrophysics of Quebec. R.J.M. is supported by NASA through the NASA Hubble Fellowship grant HST-HF2-51513.001, awarded by the Space Telescope Science Institute, which is operated by the Association of Universities for Research in Astronomy, Inc., for NASA, under contract NAS 5-26555. C. P.-G. acknowledges support from the NSERC Vanier scholarship and iREx. M.T. thanks the Gruber Foundation for its generous support to this research, acknowledges support from the Tremplin 2022 program of the Faculty of Science and Engineering of Sorbonne University, and thanks the Generic PCM team for the teamwork development and improvement of the model. This work was performed using the High-Performance Computing (HPC) resources of Centre Informatique National de l'Enseignement Supérieur (CINES) under allocation Nos. A0120110391 and A0140110391 made by Grand Équipement National de Calcul Intensif (GENCI). M.F.T. acknowledges financial support from the Clarendon Fund and the FRQNT.

Facility: JWST/NIRISS

Software: `Astropy` (Astropy Collaboration et al. 2013, 2018, 2022); `matplotlib` (Hunter 2007); `juliet` (Espinoza et al. 2019); `batman` (Kreidberg 2015); `SciPy` (Virtanen et al. 2020); `NumPy` (Harris et al. 2020); `PSG` (Villanueva et al. 2022); `SOSSISSE` (github.com/njcuk9999/sossisse); `supreme-SPOON` (github.com/radicamc/supreme-spoon); `exofile` (github.com/AntoineDarveau/exofile).

Appendix A
Data Reduction Pipelines

The NIRISS data were reduced with two independent pipelines (`SOSSISSE` and `supreme-SPOON`) briefly described here.

The `SOSSISSE` package starts with the *rateints.fits* data product issued by the Mikulski Archive for Space Telescopes (MAST) and performs custom background subtraction, flat-field correction, and $1/f$ noise correction. A high-S/N, normalized reference trace $M_{i,j}$ is then constructed from stacking the out-of-transit-corrected 2D images, with i, j the pixels in the x (dispersion) and y (cross-dispersion) directions. Here $M_{i,j}$ is limited to 30 pixels in the y-axis. In the `SOSSISSE` framework, flux is expressed as a linear combination of $M_{i,j}$ and its spatial derivatives tracing instrumental morphological changes of the trace (Equation (A1) in Lim et al. 2023), e.g., x- and y-displacement, rotation, and PSF width changes. We utilized two outputs from `SOSSISSE`: the amplitude term $a(t)$, scaling $M_{i,j}$ at each integration equivalent to the (normalized) stellar flux integrated over all pixels (WLC), and the extracted 2D spectroscopic time series for the spectrophotometric fits.

The `supreme-SPOON` pipeline works with the *uncal.fits* files available on MAST. We followed Stages 1, 2, and 3 detailed in Radica et al. (2023) and extracted the flux using a simple box aperture with a width of 30 pixels. The aperture box size was selected to minimize the variance in the out-of-transit WLC. We expect a negligible level of order contamination (order 2 onto order 1) at wavelengths above 1.6 μm for this target (Darveau-Bernier et al. 2022; Radica et al. 2022). A $1/f$ noise correction is applied following the method described in Radica et al. (2023) and Benneke et al. (2024). We, moreover, correct for the presence of the dispersed contaminant star in visit 1 using the method of Radica et al. (2023). This correction is done after flux extraction, unlike the `SOSSISSE` treatment of the contaminant, which is applied directly on the detector images (Section 2).

Figure A1 shows that the combined transmission spectra at $R \approx 100$ derived from both pipelines are in good agreement with mean (median) absolute deviations of 0.72σ (0.60σ) for LHS 1140 b and 0.58σ (0.52σ) for LHS 1140 c.

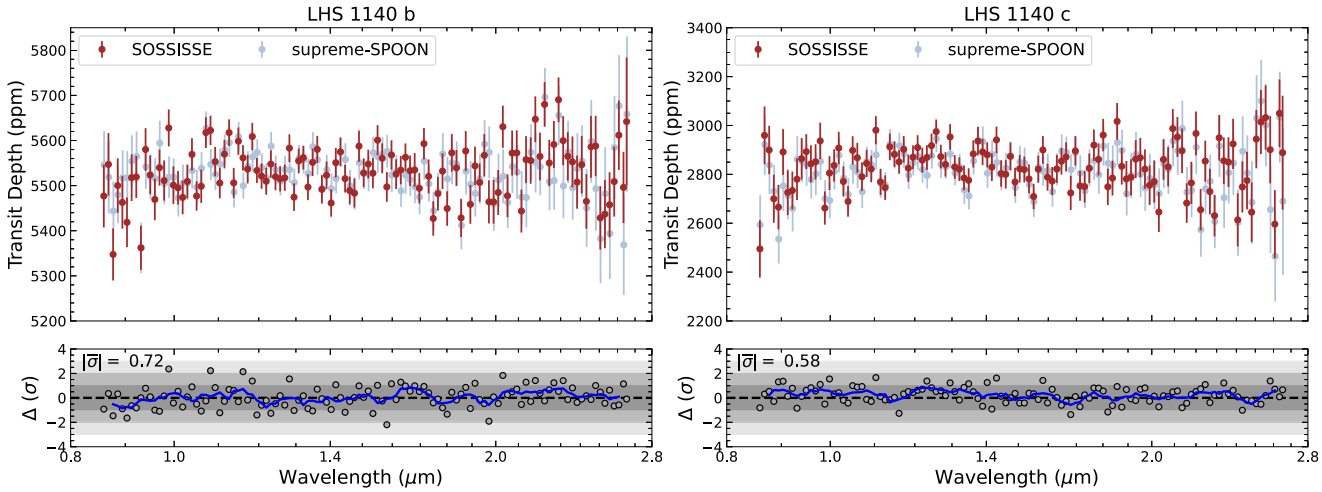

Figure A1. Combined (two visits) transmission spectrum of LHS 1140 b on the left and (one visit) transmission spectrum of LHS 1140 c on the right extracted with the `SOSSISSE` and `supreme-SPOON` pipelines, here shown for the first order of NIRISS/SOSS. The transit light-curve fitting is identical between pipelines; any differences arise during the reduction stages. The panels below show the difference in transit depths (`SOSSISSE` − `supreme-SPOON`) normalized by the maximum errors between the two pipelines at each spectral bin. A running mean (window = 5) is drawn with a blue curve showing no clear trends in the residuals. The pipelines are in good agreement with an average per-point difference of 0.72σ and 0.58σ for the spectra of LHS 1140 b and c, respectively.

Appendix B
Transmission Spectra

The final NIRISS SOSS transmission spectra ($R \approx 100$) of LHS 1140 b and c from the combined two-visit spectral extraction are given in Table B1.

Table B1
NIRISS SOSS Transmission Spectra of LHS 1140 b and c

Central Wavelength (μm)	Bandwidth (μm)	Depth b (ppm)	Error b (ppm)	Depth c (ppm)	Error c (ppm)	Order
0.65338	0.00327	5210.71	236.64	3331.44	362.37	2
0.65995	0.00330	5592.47	253.80	2247.57	397.11	2
0.66658	0.00333	5094.17	227.03	3275.11	391.74	2
0.67328	0.00337	5167.24	199.42	2676.46	374.10	2
0.68005	0.00340	5296.80	175.59	2650.32	358.80	2
0.68688	0.00343	5112.36	165.52	2645.80	321.08	2
0.69379	0.00347	5322.05	141.06	2833.85	259.10	2
…	…	…	…	…	…	…

(This table is available in its entirety in machine-readable form in the online article.)

Appendix C
Preliminary Analysis of the Transmission Data of LHS 1140 c

The first transmission spectrum of the warm super-Earth LHS 1140 c is presented in Figure C1. We present here a first exploratory analysis of LHS 1140 c's NIRISS/SOSS spectrum by repeating the retrieval exercise outlined in Section 5.2 for the Flat line, TLS-only, and TLS + Multigas (Haze) models. All priors remain unchanged except for $R_{p,\mathrm{ref}}$ and M_p, which changed to $\mathcal{U}(1, 1.5)$ and $\mathcal{N}(1.91, 0.06^2)$ based on Cadieux et al. (2024), and T, now allowed to go to higher temperatures (100–600 K).

A flat solution is favored for LHS 1140 c (2.1σ), due to the lower-S/N spectrum derived from a single transit entirely confined into a transit of LHS 1140 b (double transit; Figure 1). The Flat line model yields a $\ln \mathcal{Z} = 1090.49$, while the TLS-only and TLS + Multigas (Haze) retrieval runs end up with marginally lower Bayesian evidences of $\ln \mathcal{Z} = 1089.34$ and 1088.83, respectively.

The stellar-contamination-only model yields consistent unocculted heterogeneity properties compared to LHS 1140 b: $f_{\mathrm{fac}} = 0.12^{+0.18}_{-0.07}$ and $T_{\mathrm{fac}} = 3293^{+205}_{-111}$ K, with f_{spot} consistent with 0. The TLS effect associated with LHS 1140 c is smaller by definition given the surface ratio of the planets $(R_{p,\mathrm{c}}/R_{p,\mathrm{b}})^2$ of about one-half.

Our joint stellar contamination and planetary atmosphere retrieval (TLS + Multigas model) can inform on possible atmospheres on LHS 1140 c. The posterior distributions for this run are presented in Appendix D. We do not detect any molecular feature or a slope from hazes (haze parameters are unconstrained). The most likely composition favored by the data is a pure N_2 envelope at any T. Two other solutions exist that are approximately equally likely: a H_2O-rich atmosphere at $T \approx 200$ K, or a CO_2-rich atmosphere at $T \lesssim 500$ K. The

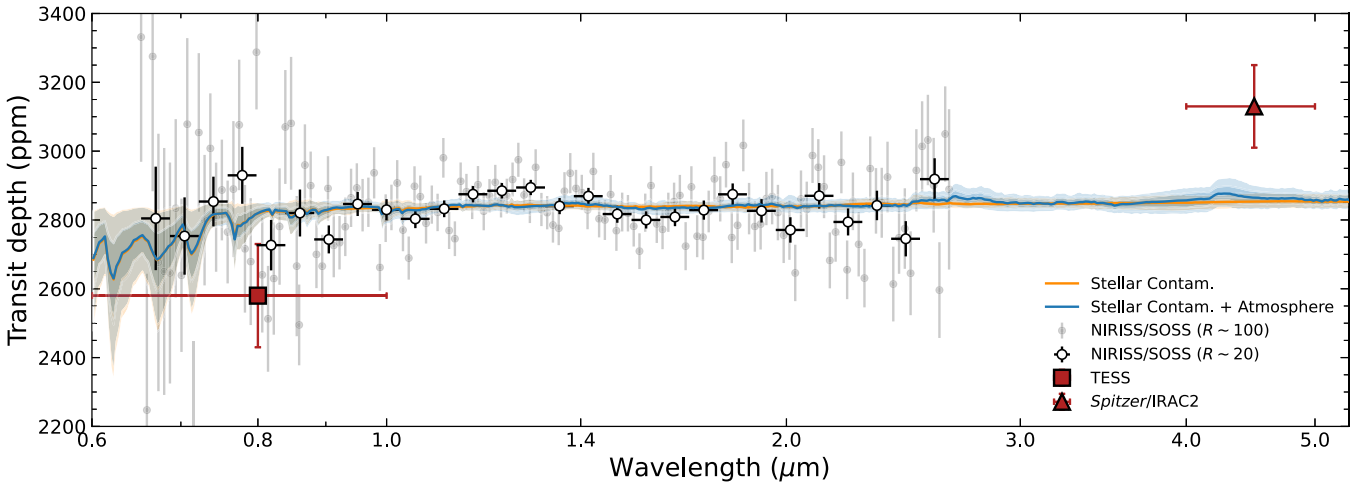

Figure C1. Transmission spectrum of LHS 1140 c from NIRISS/SOSS at an $R \sim 20$ (white points) and at a higher $R \sim 100$ (gray points). The best-fit models from `POSEIDON` with 1σ–2σ confidence envelopes are shown for a stellar contamination model (orange) and a joint stellar contamination and planetary atmosphere model (blue). The TESS and Spitzer photometric measurements (Cadieux et al. 2024) are shown in red. We have included the Spitzer point in the retrieval analysis, but its exclusion does not change the results. The NIRISS/SOSS observations are flat, with marginal evidence of unocculted faculae consistent with the simultaneous transit of LHS 1140 b (Figure 2). The spectrum covering 0.65–2.7 μm has an average transit depth that falls between those measured by TESS and Spitzer, resolving the 4σ discrepancy in radius measurements between the two instruments noted by Cadieux et al. (2024).

combination of a high mean molecular weight μ and/or low T for such atmospheres is sufficient to flatten the spectrum below the sensitivity of our NIRISS spectrum. The data are incompatible with clear CH_4-rich and H_2-rich atmospheres with 2σ upper limits of $\log CH_4 < -2.25$ and $\log H_2 < -0.94$ (<11%), respectively.

Appendix D
Supplementary Material: Atmospheric Inference Analysis

D.1. Evidence for a N_2-dominated Atmosphere on LHS 1140 b

Here we elucidate why our retrievals favor a N_2-dominated atmosphere. The observed transmission spectrum is given by $\Delta_{\lambda,\mathrm{obs}} = \epsilon_{\lambda,\mathrm{star}} \Delta_{\lambda,\mathrm{atm}}$, where $\epsilon_{\lambda,\mathrm{star}}$ is the "stellar contamination factor" (e.g., Equation (3) in Fournier-Tondreau et al. 2024) and $\Delta_{\lambda,\mathrm{atm}}$ is the "regular" transmission spectrum of the planetary atmosphere. Given that unocculted faculae are the dominant wavelength-dependent effect sculpting LHS 1140 b's transmission spectrum, we first corrected our NIRISS/SOSS data by dividing out the best-fitting unocculted stellar contamination model (binned to the resolution of the data). This allows one to compare model atmosphere-transmission-only spectra, $\Delta_{\lambda,\mathrm{atm}}$, to an equivalent form of the data.

Figure D1 compares our stellar-contamination-corrected transmission spectrum of LHS 1140 b with our best-fitting 100% N_2 and 100% CO_2 atmosphere models. The CO_2 model is essentially flat, consistent with a nondetection of CO_2 bands. The N_2 model, however, exhibits a clear Rayleigh slope in both the first and second orders of the NIRISS/SOSS data (alongside a weaker N_2–N_2 CIA feature near 2.2 μm). Both models allow for the possibility of power-law hazes, but N_2 Rayleigh scattering alone provides the necessary slope without any additional scattering opacity. We stress that the residual slope attributed here to N_2 relies on the assumption that the stellar contamination is well described by our interpolated PHOENIX models for faculae. The best TLS model leaves a significant residual near 2.3 μm, which is coincident with the CO band head, a well-known temperature- and gravity-sensitive spectral feature in M dwarf spectra. Given inherent uncertainties associated with stellar atmosphere models (e.g., Lim et al. 2023; Jahandar et al. 2024), one cannot rule out the possibility that the measured slope is an artifact of imperfect stellar contamination correction. The evidence for N_2 is only tentative at this stage (2.3σ) and will need to be confirmed with future observations.

D.2. Atmospheric and Stellar Retrieval Results

The priors, posterior parameter constraints, and key statistics from our retrieval analysis of LHS 1140 b are presented in Table D1. The full posterior distributions are shown for the TLS-only model in Figure D2, TLS + N_2 (Clear) in Figure D3, TLS + Multigas (Haze) in Figure D4, and TLS + Multigas (Haze + Cloud) in Figure D5. Finally, the posterior distributions for the TLS + Multigas (Haze) retrieval of LHS 1140 c are presented in Figure D6.

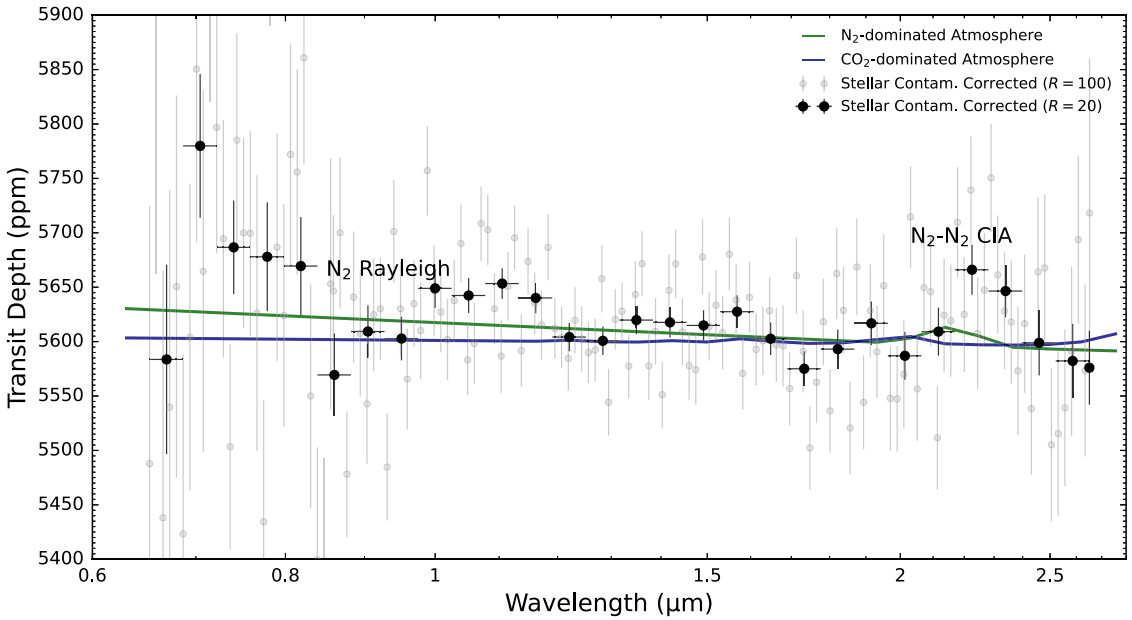

Figure D1. Tentative evidence of a N_2-dominated atmosphere on LHS 1140 b. The stellar-contamination-corrected LHS 1140 b NIRISS/SOSS transmission spectrum (black points for $R \sim 20$, gray points for $R \sim 100$) is compared with the best-fitting model transmission spectra for a 100% N_2 atmosphere (green) and a 100% CO_2 atmosphere (blue), plotted at $R = 20$. The N_2 model has a best-fitting $T = 399$ K, while the CO_2 model has $T = 116$ K. The N_2 model provides a better fit (2.3σ), due to the presence of a Rayleigh scattering slope and a weak N_2–N_2 CIA feature.

Table D1
Retrieval Analysis Summary for LHS 1140 b's Combined NIRISS/SOSS Transmission Spectrum

Parameter	Prior	Flat Line	TLS Only	TLS + N_2 (Clear)	TLS + Multigas (Haze)	TLS + Multigas (Haze + Cloud)
			Stellar Contamination			
$T_{\rm spot}$ (K)	$\mathcal{U}(2300, T_{\rm eff} + 3\sigma_{T_{\rm eff}})$	⋯	3003^{+66}_{-149}	2995^{+69}_{-146}	3017^{+60}_{-87}	3010^{+59}_{-88}
$T_{\rm phot}$ (K)	$\mathcal{N}(T_{\rm eff}, \sigma^2_{T_{\rm eff}})$	⋯	3073^{+45}_{-34}	3074^{+42}_{-33}	3076^{+43}_{-35}	3073^{+41}_{-34}
$T_{\rm fac}$ (K)	$\mathcal{U}(T_{\rm eff} - 3\sigma_{T_{\rm eff}}, 1.2\,T_{\rm eff})$	⋯	3155^{+91}_{-59}	3153^{+65}_{-49}	3146^{+64}_{-49}	3142^{+66}_{-46}
$f_{\rm spot}$	$\mathcal{U}(0, 0.5)$	⋯	$0.04^{+0.12}_{-0.03}$	$0.04^{+0.09}_{-0.03}$	$0.07^{+0.10}_{-0.05}$	$0.06^{+0.09}_{-0.05}$
$f_{\rm fac}$	$\mathcal{U}(0, 0.5)$	⋯	$0.20^{+0.17}_{-0.12}$	$0.22^{+0.15}_{-0.11}$	$0.25^{+0.15}_{-0.13}$	$0.23^{+0.14}_{-0.11}$
			Atmospheric Properties			
$R_{p,\rm ref}$ ($R_\oplus$)	$\mathcal{U}(1.5, 2.0)$	1.7513 ± 0.0006	1.762 ± 0.002	1.765 ± 0.002	1.764 ± 0.002	1.758 ± 0.005
M ($M_\oplus$)	$\mathcal{N}(5.60, 0.19^2)$	⋯	⋯	5.59 ± 0.17	5.48 ± 0.17	5.60 ± 0.16
T (K)	$\mathcal{U}(100, 400)$	⋯	⋯	331^{+45}_{-91}	290^{+76}_{-124}	224^{+103}_{-80}
$\log a_{\rm haze}$	$\mathcal{U}(-4, 8)$	⋯	⋯	⋯	$2.08^{+3.65}_{-3.80}$	$2.06^{+3.55}_{-3.56}$
$\gamma_{\rm haze}$	$\mathcal{U}(-20, 2)$	⋯	⋯	⋯	$-8.35^{+6.52}_{-7.17}$	$-8.34^{+6.32}_{-6.77}$
$\log(P_{\rm surf}/\ {\rm bar})$	$\mathcal{U}(-7, 2)$	⋯	⋯	⋯	⋯	$-3.64^{+4.12}_{-2.05}$
$\log X_{H_2}$	(derived)	⋯	⋯	⋯	< -0.95	< -0.56
$\log X_{N_2}$	$\mathcal{CLR}(-12, 0)$	⋯	⋯	0 (fixed)	$-0.00^{+0.00}_{-0.01}$	$-0.69^{+0.69}_{-6.92}$
$\log X_{CO_2}$	$\mathcal{CLR}(-12, 0)$	⋯	⋯	⋯	$-7.62^{+3.79}_{-2.67}$[a]	$-3.47^{+3.47}_{-5.25}$
$\log X_{H_2O}$	$\mathcal{CLR}(-12, 0)$	⋯	⋯	⋯	< -2.94	$-6.14^{+5.47}_{-3.74}$
$\log X_{CH_4}$	$\mathcal{CLR}(-12, 0)$	⋯	⋯	⋯	< -2.78	$-6.17^{+4.16}_{-3.41}$
			Model Statistics			
	$N_{\rm params}$	1	6	8	14	15
	χ^2 (dof)	277 (141)	235 (136)	228 (134)	228 (128)	228 (127)
	χ^2_ν	1.96	1.73	1.70	1.78	1.80
	$\ln \mathcal{Z}$	1127.24	1142.15	1144.65	1141.79	1141.60

Notes. TLS = "transit light source effect" (contamination from unocculted stellar active regions; Rackham et al. 2018). "Multigas" retrievals include N_2, H_2, CO_2, H_2O, and CH_4. $\mathcal{CLR}$ refers to the centered-log ratio prior (e.g., Benneke & Seager 2012). H_2 also follows a $\mathcal{CLR}$ prior, even though it is not a free parameter (it is derived from the summation to unity condition), since this is the defining feature of the centered-log ratio. The a priori known stellar properties are $T_{\rm eff} = 3096$ and $\sigma_{T_{\rm eff}} = 48$ K (Cadieux et al. 2024).

[a] CO_2 has a biomodal distribution, with either (i) a nondetection for a pure N_2 atmosphere or (ii) 100% CO_2 to render the spectrum flat (the latter solution is statistically disfavored). Upper bounds correspond to 95% confidence (2σ) limits. Figure 2 shows results for the "TLS-only" (orange histograms) and the "TLS + Multigas (Haze)" (blue histograms) models summarized in this table.

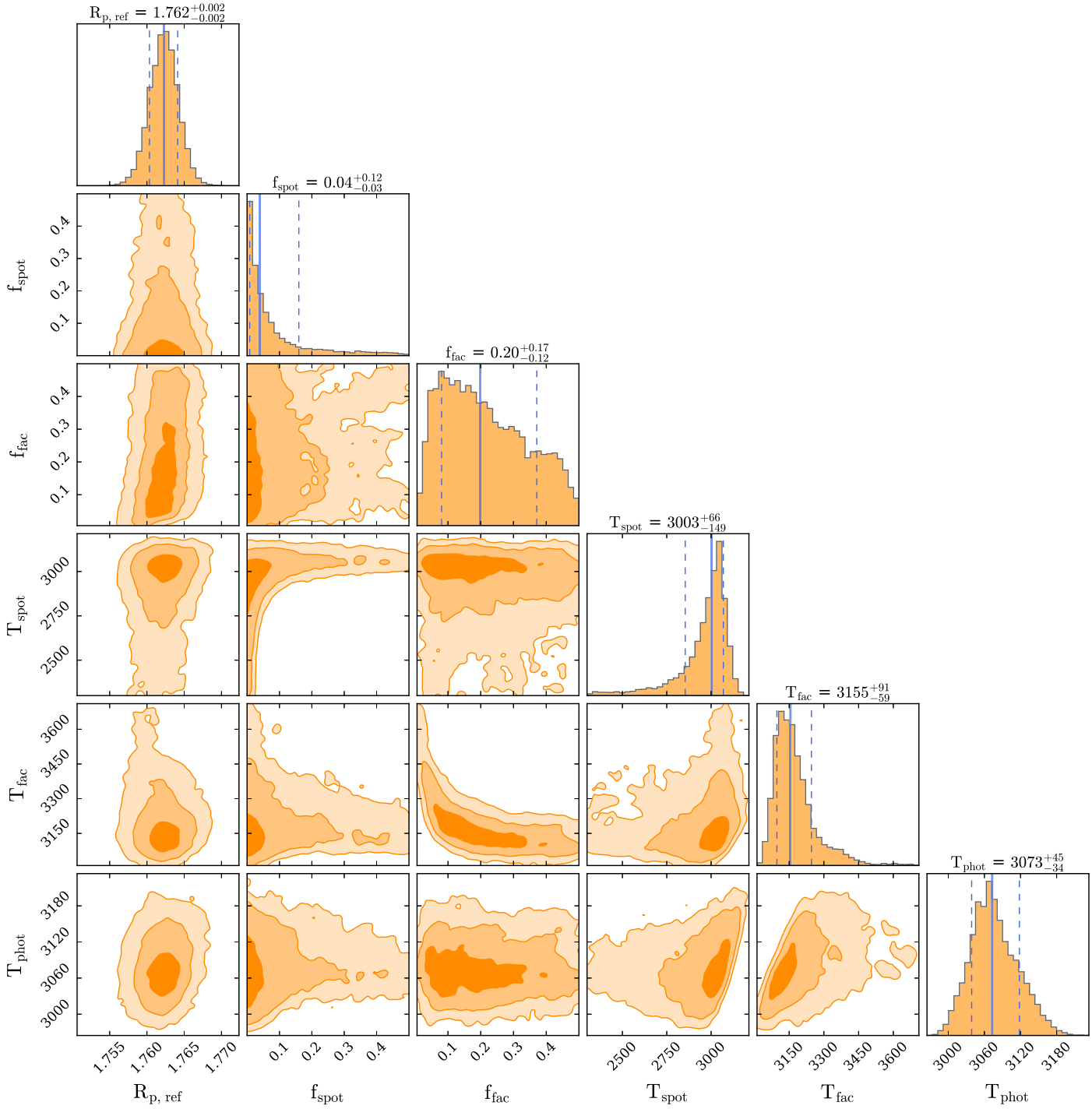

Figure D2. Posterior distribution for the stellar-contamination-only ("TLS-only") `POSEIDON` retrieval of LHS 1140 b's combined NIRISS/SOSS transmission spectrum.

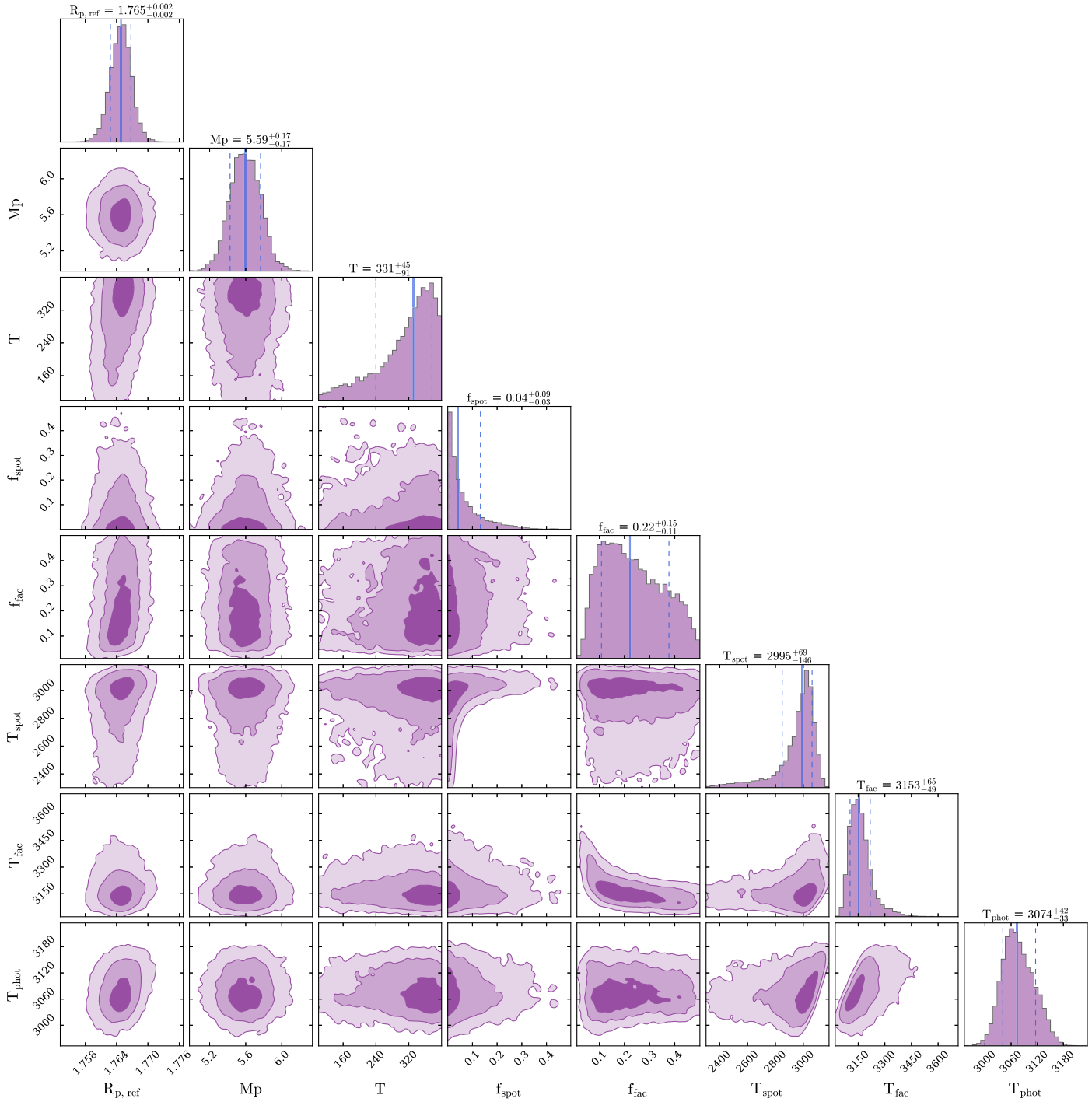

Figure D3. Posterior distribution for the joint N_2 atmosphere and stellar contamination retrieval of LHS 1140 b's combined NIRISS/SOSS transmission spectrum. Note that N_2 does not show in the corner plot as a free parameter because the N_2 abundance is fixed to 100% for this model.

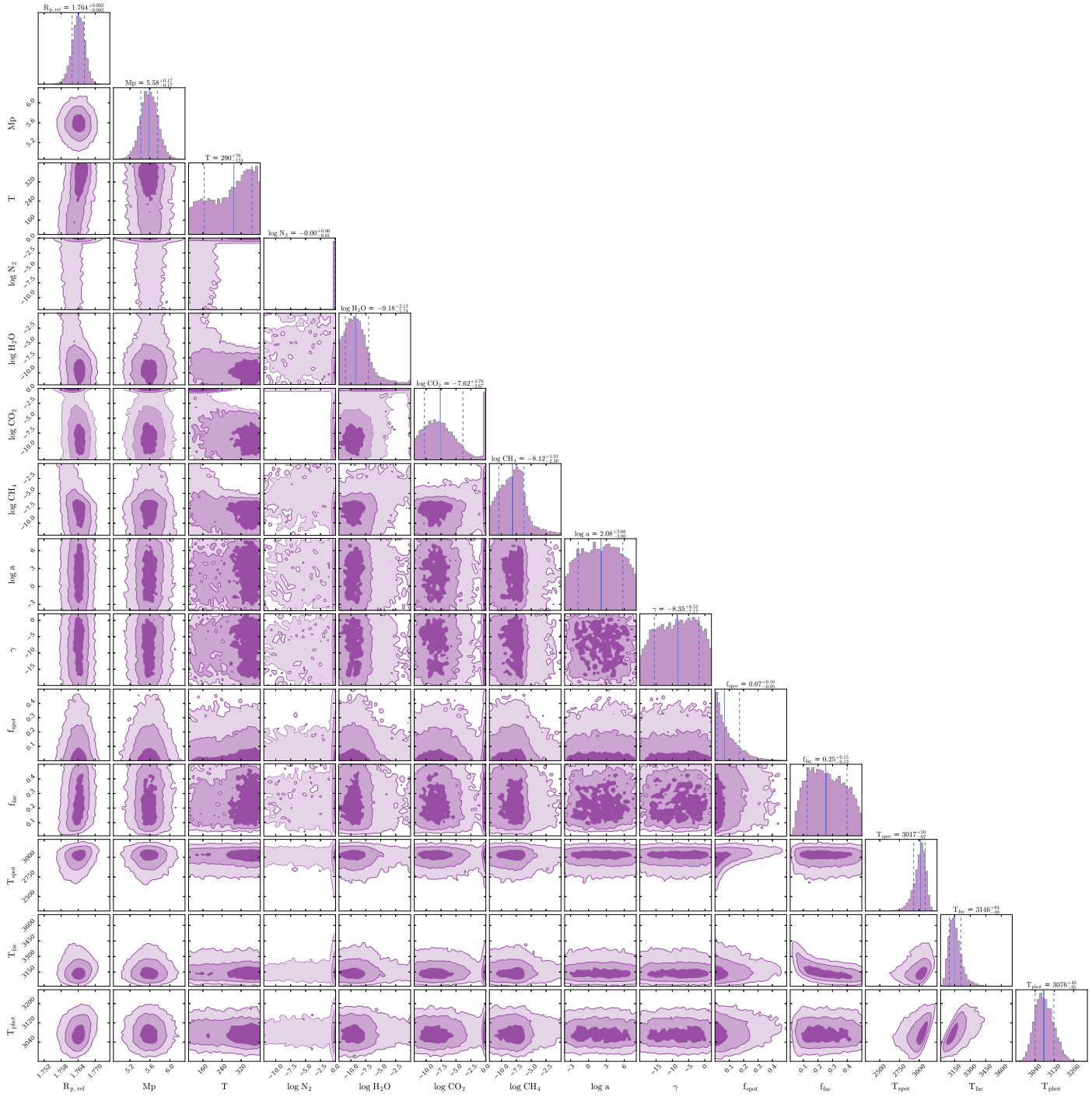

Figure D4. Posterior distribution for the joint multigas atmosphere with hazes and stellar contamination retrieval of LHS 1140 b's combined NIRISS/SOSS transmission spectrum.

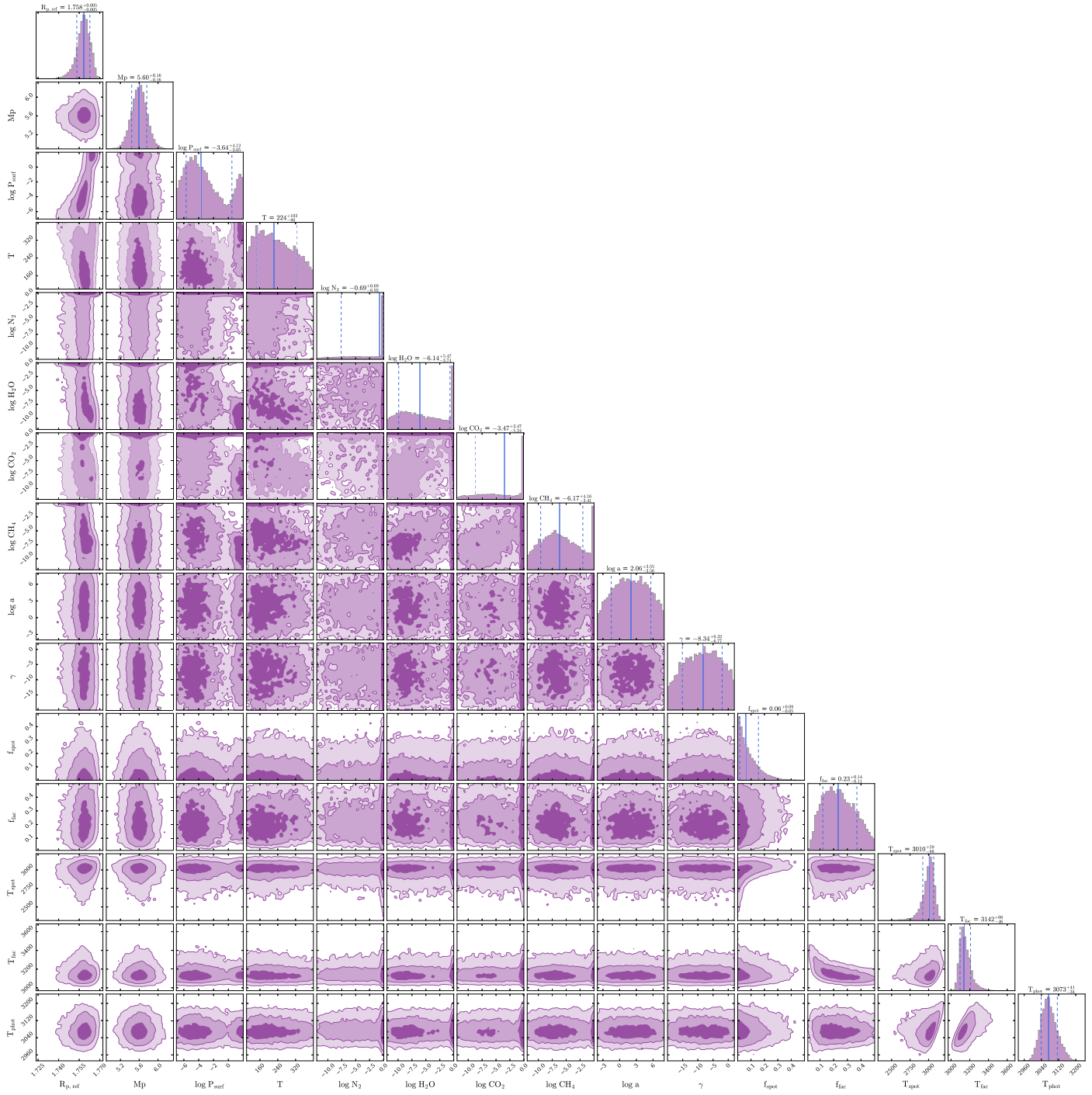

Figure D5. Posterior distribution for the joint multigas atmosphere with hazes, a cloud/surface, and stellar contamination retrieval of LHS 1140 b's combined NIRISS/SOSS transmission spectrum.

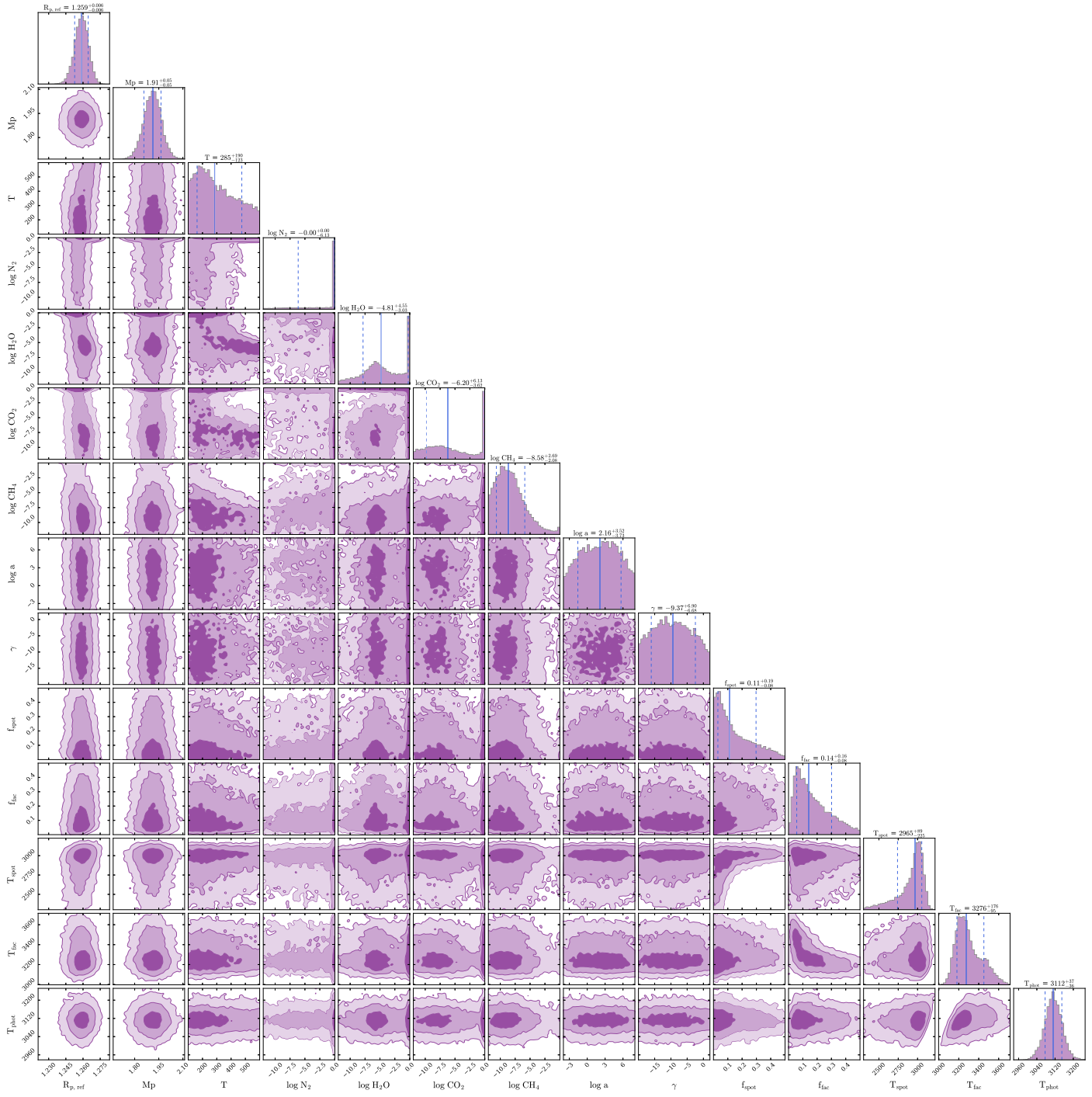

Figure D6. Posterior distribution for the joint multigas atmosphere with hazes and stellar contamination of LHS 1140 c's NIRISS/SOSS transmission spectrum.

Appendix E
Global Climate Model Simulations and Synthetic Observables

We performed a series of 3D GCM simulations designed to explore a large variety of plausible atmospheric compositions for LHS 1140 b. These simulations include (i) thick mini-Neptune atmospheres (80 bar H_2-rich) with compositions of 100×, 300×, and 1000× solar metallicity, described in the main text; (ii) compact secondary N_2- and CO_2-rich atmospheres, described in Cadieux et al. (2024); and (iii) sensitivity experiments of H_2-rich atmospheres on top of a dry surface or a global surface ocean, aka "Hycean"-type planet (Madhusudhan et al. 2021).

Figure E1 shows the temperature, water vapor mixing ratio, and cloud profiles for the mini-Neptune cases, as well as for the Earth-like and CO_2-dominated atmospheres for comparison. In all these simulations, cloud decks are located below atmospheric pressures of ∼0.1 bars, near the top of the tropospheric cold trap. Clouds therefore have a very limited impact on the transit spectra (see Figure 3) for all the simulations explored in this work. Previous intercomparison works (Fauchez et al. 2022; Sergeev et al. 2022) have shown that cloud deck altitude can vary slightly from one model to another, but here cloud

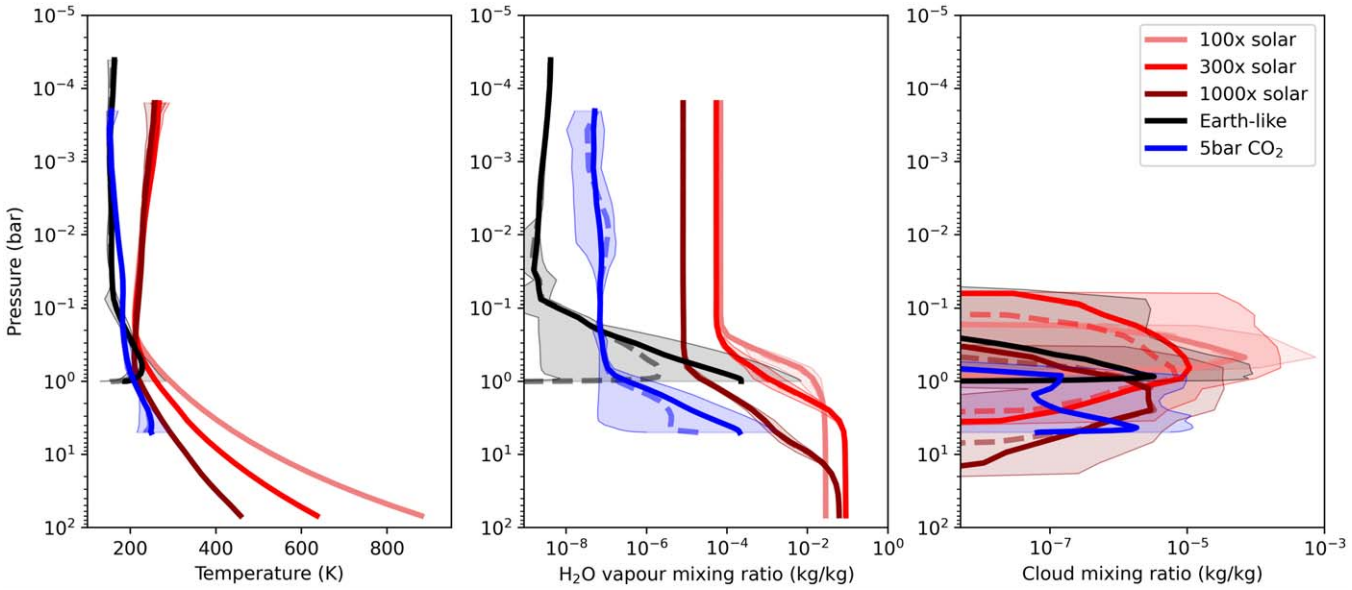

Figure E1. Results of GCM simulations of LHS 1140 b assuming mini-Neptune thick H_2 atmosphere (100×, 300×, and 1000× solar metallicity composition), an Earth-like atmosphere (1 bar N_2, 400 ppm CO_2), and a thick CO_2-dominated atmosphere (5 bar of CO_2). Panels show vertical profiles of the atmospheric temperatures (left), water vapor mixing ratio (middle), and water cloud mixing ratios (right). The thick solid lines indicate the global mean vertical profiles, and the dotted lines indicate the terminator vertical profiles (impacting transit spectra).

deck altitude would have to rise by at least two orders of magnitude to alter our conclusions. The presence of high-altitude hazes—which is not simulated here—could flatten the transit spectrum even in the case of an atmosphere rich in H_2, but in this scenario we would expect to see a haze slope in the short-wavelength part of spectrum (Sing et al. 2011).

Some simulated cases show a slight variability in the amplitude of transit spectra due to cloud variability (in time and location), as already shown in Charnay et al. (2021) in the case of K2-18 b. However, even at model time steps where the terminator region is the cloudiest, the amplitude of the transit spectrum features for the mini-Neptune cases is far greater than the scatter of NIRISS observations, so these compositions can be formally rejected.

We ran additional sensitivity simulations in which we changed the boundary conditions for the mini-Neptune simulations. First, we added a dry surface at 10-bar atmospheric pressure, but in this case the synthetic spectra (not shown) are very similar to the mini-Neptune cases (see Figure 3). Second, we added a surface entirely covered by an ocean also at 10-bar atmospheric pressure. This aquaplanet endowed with a thick H_2-dominated atmosphere, also known as a Hycean planet, has a quite different behavior. In fact, the simulation enters runaway greenhouse, which forces the ocean to evaporate and the surface temperatures to rise. This result is compatible with previous calculations of the runaway greenhouse limit for Hycean planets (Innes et al. 2023). As the simulation progresses, the amount of water vapor in the atmosphere increases at all altitude layers. The altitude of the water cloud deck also increases, similar to what has been shown already for N_2-dominated atmospheres entering the runaway greenhouse (Chaverot et al. 2023). For all the Hycean cases we have simulated, the amplitude of the spectral atmospheric features is far greater than the dispersion of the NIRISS/SOSS spectrum, even accounting for the effect of clouds. However, these runaway greenhouse simulations have, by definition, not reached their final equilibrium state, with clouds potentially forming even higher in the atmosphere. Moreover, it is not known whether the ocean at the base of the H_2-H_2O-dominated atmosphere can eventually stabilize at higher temperatures, which would also likely affect the water vapor and cloud structures. Last but not least, we have not accounted for convection inhibition, which would likely make this type of atmosphere much hotter in the lowest atmospheric layers and make it even less likely for an ocean to exist (Innes et al. 2023; Leconte et al. 2024). Performing fully converged 3D GCM simulations of Hycean planets, accounting for moist convection, clouds, and convection inhibition together at the same time, is a challenging yet necessary step (Leconte et al. 2024) to simulate accurately the evolution and stability of LHS 1140 b as a Hycean planet.

ORCID iDs

Charles Cadieux https://orcid.org/0000-0001-9291-5555
René Doyon https://orcid.org/0000-0001-5485-4675
Ryan J. MacDonald https://orcid.org/0000-0003-4816-3469
Martin Turbet https://orcid.org/0000-0003-2260-9856
Étienne Artigau https://orcid.org/0000-0003-3506-5667
Olivia Lim https://orcid.org/0000-0003-4676-0622
Michael Radica https://orcid.org/0000-0002-3328-1203
Thomas J. Fauchez https://orcid.org/0000-0002-5967-9631
Salma Salhi https://orcid.org/0000-0001-6758-7924
Lisa Dang https://orcid.org/0000-0003-4987-6591
Loïc Albert https://orcid.org/0000-0003-0475-9375
Louis-Philippe Coulombe https://orcid.org/0000-0002-2195-735X
Nicolas B. Cowan https://orcid.org/0000-0001-6129-5699
David Lafrenière https://orcid.org/0000-0002-6780-4252
Alexandrine L'Heureux https://orcid.org/0009-0005-6135-6769
Caroline Piaulet-Ghorayeb https://orcid.org/0000-0002-2875-917X
Björn Benneke https://orcid.org/0000-0001-5578-1498
Ryan Cloutier https://orcid.org/0000-0001-5383-9393

Benjamin Charnay https://orcid.org/0000-0003-0977-6545
Neil J. Cook https://orcid.org/0000-0003-4166-4121
Marylou Fournier-Tondreau https://orcid.org/0000-0002-5428-0453
Mykhaylo Plotnykov https://orcid.org/0000-0002-9479-2744
Diana Valencia https://orcid.org/0000-0003-3993-4030

References

Agol, E., Dorn, C., Grimm, S. L., et al. 2021, PSJ, 2, 1
Akeson, R. L., Chen, X., Ciardi, D., et al. 2013, PASP, 125, 989
Albert, L., Lafrenière, D., René, D., et al. 2023, PASP, 135, 075001
Allard, F., Homeier, D., & Freytag, B. 2012, RSPTA, 370, 2765
Astropy Collaboration, Price-Whelan, A. M., Lim, P. L., et al. 2022, ApJ, 935, 167
Astropy Collaboration, Price-Whelan, A. M., Sipőcz, B. M., et al. 2018, AJ, 156, 123
Astropy Collaboration, Robitaille, T. P., Tollerud, E. J., et al. 2013, A&A, 558, A33
Benneke, B., Roy, P.-A., Coulombe, L.-P., et al. 2024, arXiv:2403.03325
Benneke, B., & Seager, S. 2012, ApJ, 753, 100
Biagini, A., Cracchiolo, G., Petralia, A., et al. 2024, MNRAS, 530, 1054
Buchner, J., Georgakakis, A., Nandra, K., et al. 2014, A&A, 564, A125
Buratti, B., & Veverka, J. 1983, Icar, 55, 93
Cadieux, C., Doyon, R., Plotnykov, M., et al. 2022, AJ, 164, 96
Cadieux, C., Plotnykov, M., Doyon, R., et al. 2024, ApJL, 960, L3
Charnay, B., Blain, D., Bézard, B., et al. 2021, A&A, 646, A171
Charnay, B., Meadows, V., Misra, A., Leconte, J., & Arney, G. 2015, ApJL, 813, L1
Chaverot, G., Bolmont, E., & Turbet, M. 2023, A&A, 680, A103
Cloutier, R., & Menou, K. 2020, AJ, 159, 211
Coulombe, L.-P., Benneke, B., Challener, R., et al. 2023, Natur, 620, 292
Cowan, N. B., Greene, T., Angerhausen, D., et al. 2015, PASP, 127, 311
Damiano, M., Bello-Arufe, A., Yang, J., & Hu, R. 2024, ApJL, 968, L22
Darveau-Bernier, A., Albert, L., Talens, G. J., et al. 2022, PASP, 134, 094502
de Wit, J., Doyon, R., Rackham, B. V., et al. 2023, arXiv:2310.15895
Diamond-Lowe, H., Berta-Thompson, Z., Charbonneau, D., Dittmann, J., & Kempton, E. M. R. 2020, AJ, 160, 27
Dittmann, J. A., Irwin, J. M., Charbonneau, D., et al. 2017, Natur, 544, 333
Doyon, R. 2024, arXiv:2403.12617
Doyon, R., Willott, C. J., Hutchings, J. B., et al. 2023, PASP, 135, 098001
Ducrot, E., Lagage, P.-O., Min, M., et al. 2023, Combined analysis of the 12.8 and 15 microns JWST/MIRI eclipse observations of TRAPPIST-1 b, 06 December 2023, PREPRINT (v1) available at Research Square, doi:10.21203/rs.3.rs-3706919/v1
Edwards, B., Changeat, Q., Mori, M., et al. 2021, AJ, 161, 44
Espinoza, N., Kossakowski, D., & Brahm, R. 2019, MNRAS, 490, 2262
Esteves, L. J., De Mooij, E. J. W., & Jayawardhana, R. 2013, ApJ, 772, 51
Fauchez, T. J., Turbet, M., Villanueva, G. L., et al. 2019, ApJ, 887, 194
Fauchez, T. J., Villanueva, G. L., Sergeev, D. E., et al. 2022, PSJ, 3, 213
Feinstein, A. D., Radica, M., Welbanks, L., et al. 2023, Natur, 614, 670
Feroz, F., & Hobson, M. P. 2008, MNRAS, 384, 449
Foreman-Mackey, D., Agol, E., Ambikasaran, S., & Angus, R. 2017, AJ, 154, 220
Forget, F., & Leconte, J. 2014, RSPTA, 372, 20130084
Fournier-Tondreau, M., MacDonald, R. J., Radica, M., et al. 2024, MNRAS, 528, 3354
Fulton, B. J., Petigura, E. A., Blunt, S., & Sinukoff, E. 2018, PASP, 130, 044504
Fulton, B. J., Petigura, E. A., Howard, A. W., et al. 2017, AJ, 154, 109
Gaia Collaboration, Vallenari, A., Brown, A. G. A., et al. 2023, A&A, 674, A1
Gardner, J. P., Mather, J. C., Abbott, R., et al. 2023, PASP, 135, 068001
Ginzburg, S., Schlichting, H. E., & Sari, R. 2018, MNRAS, 476, 759
Gomes, G. O., & Ferraz-Mello, S. 2020, MNRAS, 494, 5082
Grant, D., & Wakeford, H. R. 2022, Exo-TiC/ExoTiC-LD: ExoTiC-LD v3.0.0, Zenodo, doi:10.5281/zenodo.7437681
Greene, T. P., Bell, T. J., Ducrot, E., et al. 2023, Natur, 618, 39
Grunblatt, S. K., Huber, D., Gaidos, E., et al. 2017, AJ, 154, 254
Harris, C. R., Millman, K. J., van der Walt, S. J., et al. 2020, Natur, 585, 357
Hohm, U. 1994, CP, 179, 533
Howard, W. S., Kowalski, A. F., Flagg, L., et al. 2023, ApJ, 959, 64
Hunter, J. D. 2007, CSE, 9, 90
Husser, T. O., Wende-von Berg, S., Dreizler, S., et al. 2013, A&A, 553, A6
Ih, J., Kempton, E. M. R., Whittaker, E. A., & Lessard, M. 2023, ApJL, 952, L4
Innes, H., Tsai, S.-M., & Pierrehumbert, R. T. 2023, ApJ, 953, 168
Irwin, J., Charbonneau, D., Nutzman, P., & Falco, E. 2009, IAU Symp. 253, Transiting Planets (Cambridge: Cambridge Univ. Press), 37
Jahandar, F., Doyon, R., Artigau, É., et al. 2024, ApJ, 966, 56
Kallinger, T., De Ridder, J., Hekker, S., et al. 2014, A&A, 570, A41
Karman, T., Gordon, I. E., van der Avoird, A., et al. 2019, Icar, 328, 160
Kempton, E. M. R., Bean, J. L., Louie, D. R., et al. 2018, PASP, 130, 114401
Kiman, R., Schmidt, S. J., Angus, R., et al. 2019, AJ, 157, 231
Kipping, D. M. 2013, MNRAS, 435, 2152
Kite, E. S., & Barnett, M. N. 2020, PNAS, 117, 18264
Kite, E. S., & Ford, E. B. 2018, ApJ, 864, 75
Kopparapu, R. K., Ramirez, R., Kasting, J. F., et al. 2013, ApJ, 765, 131
Kreidberg, L. 2015, PASP, 127, 1161
Leconte, J., Spiga, A., Clément, N., et al. 2024, A&A, 686, A131
Lillo-Box, J., Figueira, P., Leleu, A., et al. 2020, A&A, 642, A121
Lim, O., Benneke, B., Doyon, R., et al. 2023, ApJL, 955, L22
Lincowski, A. P., Meadows, V. S., Zieba, S., et al. 2023, ApJL, 955, L7
MacDonald, R. J. 2023, JOSS, 8, 4873
MacDonald, R. J., & Madhusudhan, N. 2017, MNRAS, 469, 1979
Madhusudhan, N., Piette, A. A. A., & Constantinou, S. 2021, ApJ, 918, 1
Madhusudhan, N., Sarkar, S., Constantinou, S., et al. 2023, ApJL, 956, L13
Marounina, N., & Rogers, L. A. 2020, ApJ, 890, 107
May, E. M., MacDonald, R. J., Bennett, K. A., et al. 2023, ApJL, 959, L9
McElwain, M. W., Feinberg, L. D., Perrin, M. D., et al. 2023, PASP, 135, 058001
Medina, A. A., Winters, J. G., Irwin, J. M., & Charbonneau, D. 2022, ApJ, 935, 104
Ment, K., Dittmann, J. A., Astudillo-Defru, N., et al. 2019, AJ, 157, 32
Moran, S. E., Stevenson, K. B., Sing, D. K., et al. 2023, ApJL, 948, L11
Owen, J. E., & Wu, Y. 2017, ApJ, 847, 29
Pecaut, M. J., & Mamajek, E. E. 2013, ApJS, 208, 9
Pereira, F., Campante, T. L., Cunha, M. S., et al. 2019, MNRAS, 489, 5764
Polyansky, O. L., Kyuberis, A. A., Zobov, N. F., et al. 2018, MNRAS, 480, 2597
Rackham, B. V., Apai, D., & Giampapa, M. S. 2018, ApJ, 853, 122
Radica, M., Albert, L., Taylor, J., et al. 2022, PASP, 134, 104502
Radica, M., Coulombe, L.-P., Taylor, J., et al. 2024, ApJL, 962, L20
Radica, M., Welbanks, L., Espinoza, N., et al. 2023, MNRAS, 524, 835
Ricker, G. R., Winn, J. N., Vanderspek, R., et al. 2015, JATIS, 1, 014003
Sergeev, D. E., Fauchez, T. J., Turbet, M., et al. 2022, PSJ, 3, 212
Sing, D. K., Pont, F., Aigrain, S., et al. 2011, MNRAS, 416, 1443
Sneep, M., & Ubachs, W. 2005, JQSRT, 92, 293
Speagle, J. S. 2020, MNRAS, 493, 3132
Tashkun, S. A., & Perevalov, V. I. 2011, JQSRT, 112, 1403
Townsend, R., & Lopez, A. 2023, JOSS, 8, 4602
Trotta, R. 2008, ConPh, 49, 71
Turbet, M., Bolmont, E., Leconte, J., et al. 2018, A&A, 612, A86
Turbet, M., Fauchez, T. J., Leconte, J., et al. 2023, A&A, 679, A126
Villanueva, G. L., Liuzzi, G., Faggi, S., et al. 2022, Fundamentals of the Planetary Spectrum Generator (Greenbelt, MD: Library of Congress)
Villanueva, G. L., Smith, M. D., Protopapa, S., Faggi, S., & Mandell, A. M. 2018, JQSRT, 217, 86
Virtanen, P., Gommers, R., Oliphant, T. E., et al. 2020, NatMe, 17, 261
Yurchenko, S. N., Amundsen, D. S., Tennyson, J., & Waldmann, I. P. 2017, A&A, 605, A95
Zahnle, K. J., & Catling, D. C. 2017, ApJ, 843, 122
Zechmeister, M., & Kürster, M. 2009, A&A, 496, 577
Zieba, S., Kreidberg, L., Ducrot, E., et al. 2023, Natur, 620, 746